J. Fluid Mech. (2023), *vol*. 960, A31, doi:10.1017/jfm.2023.155

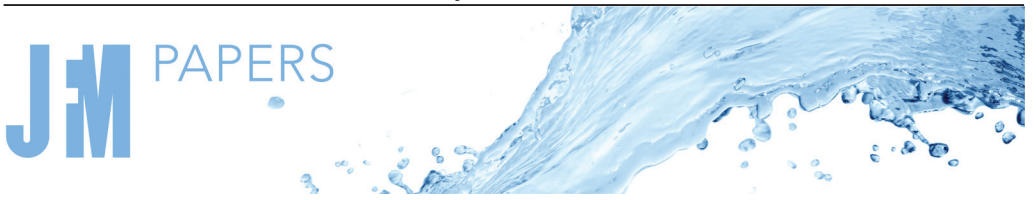

Two-dimensional study on the motion and interactions of squirmers under gravity in a vertical channel

Deming Nie[1], **Yuxiang Ying**[1], **Geng Guan**[1], **Jianzhong Lin**[2,3,†] **and Zhenyu Ouyang**[2]

[1]Institute of Fluid Mechanics, China Jiliang University, Hangzhou 310018, PR China

[2]Key Laboratory of Impact and Safety Engineering (Ningbo University), Ministry of Education, Ningbo 315201, PR China

[3]Institute of Fluid Engineering, Zhejiang University, Hangzhou 310027, PR China

(Received 13 July 2022; revised 10 January 2023; accepted 12 February 2023)

We simulated the motions and interactions of circular squirmers under gravity in a two-dimensional channel at finite fluid inertia, aiming to provide a comprehensive analysis of the dynamic features of swimming microorganisms or engineered microswimmers. In addition to a squirmer-type factor (β), another control parameter (α) was introduced, representing ratio of the self-propelling strength to the sedimentation strength of squirmers. Simulations were performed at $0.4 \leq \alpha \leq 1.2$ and $-5 \leq \beta \leq 5$. We first considered the sedimentation of a single squirmer. Five patterns were revealed, depending on both α and β: steady downward falling, steady inclined falling or rising and small-scale or large-scale oscillating. Compared with a pusher ($\beta < 0$, gaining thrust from rear), a puller ($\beta > 0$, gaining thrust from front) is more likely to break down its symmetrical structure and subsequently lose stability, owing to the high-pressure regions on its lateral sides. Typically, a pusher settles faster than a puller, whereas a neutral squirmer ($\beta = 0$) settles in between. This is related to the 'trailing negative flow' behind a pusher and 'leading negative flow' before a puller. We then placed two squirmers in line with the gravity direction to study their interactions. Results show pullers attract each other and come into contact as a result of the low-pressure regions between them, whereas the opposite is observed for pushers. The interactions between two pullers are illustrated by their respective patterns. In contrast, pushers never come into contact and maintain distance from each other with increasing separation. We finally examined how a puller interacts with a pusher.

Key words: micro-organism dynamics, suspensions, particle/fluid flows

† Email address for correspondence: mecjzlin@public.zju.edu.cn

1. Introduction

Swimming microorganisms or artificial microswimmers, driven by various self-propelling mechanisms, display rich and complex dynamic features relative to passive particles when immersed in a Newtonian fluid. For instance, the alga *Chlamydomonas reinhardtii*, swimming forward through its two flagella, undergoes an unusual 'run-and-tumble' motion in the dark, owing to its flagellar switching between synchronous and asynchronous beating (Polin *et al.* 2009). The bacteria *Bacillus subtilis* exhibits striking collective behaviours associated with hydrodynamic interactions when oxygen is available. They can power submillimetre gears with their asymmetric teeth to rotate in the direction of the teeth's slanted edges (Sokolov *et al.* 2009). The same active organisms were also found to self-organize into a single vortex and form a steady unidirectional circulation in a cylindrical chamber, with unexpected observations of the resultant fluid flows moving in the opposite direction (Lushi, Wioland & Goldstein 2014; Wioland, Lushi & Goldstein 2016). The self-assembly behaviours of motile *Escherichia coli* were observed and successfully adopted to generate a unidirectional rotation of nanofabricated objects (also termed bacterial ratchet motors in Di Leonardo *et al.* (2010)). The same microorganisms (*E. coli*) were also found to exhibit circular trajectories adjacent to surfaces and be able to sense the surface slip on the nanoscale (Hu *et al.* 2015). More interestingly, Drescher *et al.* (2009) reported a 'dancing' behaviour pattern for two algal *Volvox* colonies swimming close to a wall. The two *Volvox* colonies initially attracted each other, and then performed a 'waltz' or 'minuet' around one another (Drescher *et al.* 2009). The unusual behaviour exhibited by microorganisms swimming in viscous environments raises several issues associated with fluid dynamics. Concerning this, a series of review papers (Pedley & Kessler 1992; Lauga & Powers 2009; Koch & Subramanian 2011; Elgeti, Winkler & Gompper 2015; Saintillan 2018) focusing on different aspects of microorganisms or engineering microswimmers swimming in fluids is recommended.

Classical squirmer models (Lighthill 1952; Blake 1971*a*,*b*) have been widely adopted to describe representative microorganisms (e.g. *B. subtilis*, *C. reinhardtii*, *E. coli* and *Volvox*) in numerical and theoretical studies. A prescribed tangential slip velocity is usually applied to the surface of a squirmer (Lighthill 1952; Blake 1971*a*,*b*). Accordingly, squirmers gaining thrust from the front or rear are termed pullers or pushers, respectively. These two types of self-propelling mechanisms may cause significant differences in the structure of the flows surrounding different squirmers, and give rise to distinct dynamic features for pullers and pushers. Chisholm *et al.* (2016) numerically studied the flows around a squirmer for Reynolds numbers (Re) ranging between 0.01 and 1000, and showed that an axisymmetric flow remains stable for a pusher at Re values of at least up to 1000; moreover, the swimming velocity always increases with Re. In contrast, flow instability may occur for a puller at a large Re, leading to a drop in its swimming velocity (Chisholm *et al.* 2016). This is qualitatively consistent with the observations of Li, Ostace & Ardekani (2016). Generally, gravity has significant influences on the swimming motions of microorganisms. When microorganisms are immersed in a liquid, they usually respond to gravitational acceleration with behaviours known as gravitaxis or geotaxis. For example, gravitaxis causes many organisms (e.g. phototactic algae) to swim vertically upward on average in still water (Pedley & Kessler 1992). To shed light on this issue, numerical studies have been conducted using squirmer models. Rühle *et al.* (2018) used a method based on multi-particle collision dynamics (MPCD) to simulate the settling of a spherical squirmer under gravity between two flat walls at low Reynolds numbers. They summarized two states for the squirmer: a cruising state in a squirmer propulsion-dominated regime, and a residing state in a gravity-dominated regime (Rühle *et al.* 2018). This study also revealed

that, when a squirmer resides in the proximity of a bottom wall, it exhibits different motion patterns strongly dependent on the squirmer type. This is consistent with the observations of Fadda, Molina & Yamamoto (2020), who resolved the flow surrounding a spherical squirmer settling toward a wall under gravity through three-dimensional simulations. In particular, Fadda *et al.* (2020) considered the effects of the chirality of the squirmer to better model real microorganisms, such as *E. coli*. The squirmer was shown to undergo a circular motion in the presence of chirality instead of a straight motion (Fadda *et al.* 2020). Recently, Ouyang & Lin (2022) presented a two-dimensional analysis of the settling of a squirmer in a narrow channel. Four types of motion resulting from the hydrodynamic interactions and collisions between the squirmer and channel walls were summarized: vertical, attracted, oscillatory and upward modes. The oscillatory mode only occurs for pushers or neutral squirmers, whereas the vertical mode is not observed for pushers (Ouyang & Lin 2022). In particular, their work showed that a puller swims faster than a pusher at small squirmer-to-fluid density ratios, whereas the opposite is true at large squirmer-to-fluid density ratios (Ouyang & Lin 2022).

Moreover, significant efforts have been devoted to studying the hydrodynamic interactions between squirmers, similar to the case with passive particles. Studies have shown that these hydrodynamic interactions play key roles in the collective behaviours of swimming microorganisms, such as bioconvection (Hill & Pedley 2005; Hwang & Pedley 2014), self-organization (Lushi *et al.* 2014; Wioland *et al.* 2016), phase separation (Matas-Navarro *et al.* 2014; Theers *et al.* 2018; Lin & Gao 2019) and ordering and aggregation (Li & Ardekani 2014; Kyoya *et al.* 2015). In addition, the hydrodynamic interactions are also primarily responsible for the novel properties of a suspension of bacteria, for example, reductions in viscosity, increases in diffusivity and the extraction of useful energy (Sokolov & Aranson 2012). Ishikawa, Simmonds & Pedley (2006) presented a pioneering study on the interactions between two spherical squirmers at low Reynolds numbers. In this work, analytical expressions were approximately derived for the limits of small and large separations on the basis of lubrication theory, and agreed well with their numerical results (Ishikawa *et al.* 2006). Based on an analysis, Ishikawa *et al.* (2006) provided a database for calculating the forces exerted on either of two interacting squirmers at a given relative position and orientation. In general, their work showed that a pair of squirmers first attract each other, and come into close contact. The squirmers then change their orientation dramatically and eventually separate from each other (Ishikawa *et al.* 2006). This significantly differs from the interactions between passive particles. Papavassiliou & Alexander (2017) used the Lorentz reciprocal theorem for a Stokes flow to develop analytical solutions for a squirmer swimming close to a planar or spherical wall, as well as for the interactions between two squirmers. Their solutions could account for any type of squirmer motion at the Stokes flow limit, and were valid at any separation (Papavassiliou & Alexander 2017). Accordingly, Ishikawa *et al.* (2007) simulated the interactions between two swimming bacteria in an infinite fluid at the Stokes flow limit. Each bacterium was modelled as a spherical squirmer with a single helical flagellum. Similar to Ishikawa *et al.* (2006), their study showed that the two bacteria always avoid each other, i.e. by considerably changing their orientations as they come close to each other. This avoidance and escape behaviour was also reported for two swimming *Paramecia caudatum* between two flat plates in an experimental study (Ishikawa & Hota 2006). As indicated by Pooley, Alexander & Yeomans (2012), the interactions between two squirmers at low Reynolds numbers consist of two parts: a passive term unrelated to the motion of the second squirmer, and an active term caused by the simultaneous swimming actions of both squirmers. Consequently, the motion of

squirmers can be attractive, repulsive or oscillatory (Pooley *et al.* 2012). This is consistent with the numerical study by Mirzakhanloo, Jalali & Alam (2018), who simulated the interactions of two artificial microswimmers (*Quadroar*). Using the MPCD, Theers *et al.* (2016) investigated the interactions of a pair of spheroidal squirmers in a narrow slit and found two pullers will form a wedge-like structure with a small constant angle. Similarly, Qi *et al.* (2022) studied the collective motion of squirmers in a narrow slit and revealed that at high concentrations clusters of pushers may exhibit swarming behaviour and active turbulence resulting from the hydrodynamic interactions. Qi *et al.* (2022) also proposed some criteria to classify the active turbulence.

Fluid inertia may result in a significant difference between interacting squirmers. By using beat patterns for the bull spermatozoa (Friedrich *et al.* 2010) and for the *E. coli* (Geyer *et al.* 2013), Klindt & Friedrich (2015) computed the time-dependent fluid flow around a *Chlamydomonas* cell swimming in water by solving nonlinear Navier–Stokes equations. Their work indicated that the oscillatory flows induced by the flagellated green algae were screened by fluid inertia beyond a typical distance from this swimmer. The inertial effects could not be neglected when considering the hydrodynamic interactions between swimmers or between swimmers and boundaries. Li *et al.* (2016) numerically studied the hydrodynamic interactions of squirmers at $Re \sim O(0.1\text{–}100)$ in an unbounded fluid. They revealed that the contact time of two pushers is reduced as the fluid inertia becomes strong, whereas a pair of pullers remain close to each other for a long time. This finding is useful for exploring predator–prey interactions and sexual reproduction in the natural world. Lin & Gao (2019) examined the inertial effects on the collective behaviours of squirmers through a direct-forcing fictitious domain method, and found that fluid inertia suppresses the collective dynamics of both pushers and pullers. This action, however, is helpful for enhancing the biogenic mixing of microorganisms (Wang & Ardekani 2012, 2015). Recently, the interactions between two squirmers at a finite and intermediate inertia in a stratified fluid have been numerically examined (More & Ardekani 2021). They reported that stratification eliminates the closed-loop trajectories observed for two pullers at an intermediate fluid inertia, and makes two pushers come to a complete stop and stick to each other (More & Ardekani 2021).

Despite the significant progress made in the past, studies on swimming microorganisms in the presence of an external force (i.e. a gravitational, magnetic or chemical gradient force) remain limited. This is particularly true when the significance of gravity is considered. Under the influence of gravity, a suspension of phototactic algae slightly denser than water has an average motion of swimming upward in still water. This may lead to bioconvection when the upper regions of the suspension become denser than the lower regions (Hill & Pedley 2005). The mechanism for algae swimming upward is associated with gravity; that is, they are bottom-heavy, and therefore experience gravitational torque when they are not vertical (Pedley & Kessler 1992). Several rational continuum models have been developed to describe bioconvection exhibited by different species of microorganisms. However, significant challenges remain when it comes to swimming bacteria, and there is a need for an appropriate macroscopic model for the unique pattern formations (whorls and jets) that also considers the cell–cell interactions (Hill & Pedley 2005). In this context, gravity plays a key role in determining the swimming behaviours of certain organisms that are usually immersed in water and have a gravity-sensing-like function. For instance, *Loxodes* have an internal weighted lever whose position (along with the local oxygen concentration) controls the swimming direction (Fenchel & Finlay 1986). For phototactic flagellates such as *Euglena gracilis*, gravity considerably contributes to their vertical motion in water, enabling them to adjust their amount of exposure to solar radiation (Ntefidou *et al.* 2003). Understanding how these species interact with each other

in the presence of gravity and how they respond to an external gravitational field provides insights into the design of artificial or engineered microswimmers with gravity-sensing devices. Another relevant issue concerns the gravity-dependent orientations of certain aquatic microorganisms, as these show interesting alignments in different media. For example, Mogami, Ishii & Baba (2001) showed that immobilized *Paramecium caudatum* and gastrula larvae swim upward while falling in a hypodensity medium, and swim downward while rising in a hyperdense medium. Immobilized pluteus larvae swim upward regardless of the density of the medium (Mogami *et al.* 2001). The underlying mechanism for this biased behaviour remains under discussion, and a universal rational model has yet to be developed (Roberts 2010; Wolff, Hahn & Stark 2013; ten Hagen *et al.* 2014). More strikingly, Sengupta, Carrara & Stocker (2017) showed that some phytoplankton species (e.g. *Heterosigma akashiwo*) which usually undertake vertical migrations to gain access to nutrient-rich deep water using gravitaxis can actively modulate the cell's fore–aft asymmetry and diversify their direction of migration in response to damaging turbulent conditions. However, their experiments (Sengupta *et al.* 2017) indicate that other phytoplankton species may response to turbulence differently, which yet requires an overall understanding of the dynamic features of microorganisms in complex flow environments. In view of this, we aimed to provide a comprehensive analysis of the motion behaviours and interactions of microorganisms under gravity. To achieve this, we adopted the two-dimensional squirmer model proposed by Blake (1971*b*) for simplicity, and performed extensive simulations of the sedimentation of a single squirmer and two interacting squirmers in a vertical channel at a finite fluid inertia. The two-dimensional squirmer model has been widely adopted in previous studies (Matas-Navarro *et al.* 2014; Ouyang, Lin & Ku 2018; Ahana & Thampi 2019; Ouyang & Lin 2022). We hope our fully resolved hydrodynamics will provide a general understanding of the dynamic features of swimming squirmers under the influence of gravity, as well as helping to explain the characteristics of the fluid flows created by the squirmers.

The remainder of this paper is organized as follows. In § 2, we briefly introduce the lattice Boltzmann method (LBM) and our treatments of the boundary conditions. The two-dimensional squirmer model and collision strategy used are also discussed in this section. The physical model and control parameters are presented in § 3. In § 4, we provide two benchmark tests to ensure that the LBM method, along with our settings, can accurately solve the motions of squirmer settings under gravity. The numerical results, including the motion of a single squirmer and interactions between two pullers, as well as those between two pushers, are provided and discussed in § 5. In particular, we show how a puller interacts with a pusher. Concluding remarks are provided in § 6.

2. Numerical method

2.1. *Lattice Boltzmann method*

In this study, the motion of the fluid was solved through a single-relaxation-time LBM (Qian 1992). The discrete lattice Boltzmann equations are as follows:

$$f_i(\boldsymbol{x} + \boldsymbol{e}_i\Delta t, t + \Delta t) - f_i(\boldsymbol{x}, t) = -\frac{1}{\tau}[f_i(\boldsymbol{x}, t) - f_i^{(eq)}(\boldsymbol{x}, t)]. \tag{2.1}$$

In the above, $f_i\ (\boldsymbol{x}, t)$ is the density distribution function along the direction $\boldsymbol{e}_i$ at $(\boldsymbol{x}, t)$, and $f_i^{(eq)}(\boldsymbol{x}, t)$ denotes the corresponding equilibrium distribution function; Δt is the time step of the simulation, and τ is a relaxation time related to the fluid viscosity ν. The fluid

density ρ and velocity $\boldsymbol{u}$ are determined as follows:

$$\rho = \sum_i f_i, \quad \rho \boldsymbol{u} = \sum_i f_i \boldsymbol{e}_i. \tag{2.2a,b}$$

The popular D2Q9 (i.e. nine discrete velocities in two dimensions) lattice model was adopted (Qian 1992). Accordingly, the discrete velocity vectors on a square lattice are given as follows:

$$\boldsymbol{e}_i = \begin{cases} (0, 0), & \text{for } i = 0 \\ (\pm 1, 0)c, (0, \pm 1)c, & \text{for } i = 1 \text{ to } 4 \\ (\pm 1, \pm 1)c, & \text{for } i = 5 \text{ to } 8 \end{cases}. \tag{2.3}$$

In the above, Δx is the lattice grid, and $c = \Delta x/\Delta t$ represents the lattice speed. Following Qian (1992), we choose the equilibrium distribution functions as follows:

$$f_i^{(eq)}(\boldsymbol{x}, t) = w_i \rho \left[1 + \frac{3\boldsymbol{e}_i \cdot \boldsymbol{u}}{c^2} + \frac{9(\boldsymbol{e}_i \cdot \boldsymbol{u})^2}{2c^4} - \frac{3\boldsymbol{u}^2}{2c^2} \right]. \tag{2.4}$$

Here, w_i are the weights; $w_0 = 4/9$, $w_{1\text{–}4} = 1/9$ and $w_{5\text{–}8} = 1/36$. Notably, in the D2Q9 model, the speed of sound has a relationship of $c_s = c/\sqrt{3}$.

By performing a Chapman–Enskog expansion, the macroscopic mass and momentum equations at the low Mach number limit can be recovered as follows:

$$\frac{\partial \rho}{\partial t} + \nabla \cdot (\rho \boldsymbol{u}) = 0, \tag{2.5}$$

$$\frac{\partial (\rho \boldsymbol{u})}{\partial t} + \nabla \cdot (\rho \boldsymbol{u}\boldsymbol{u}) = -\nabla p + \rho \nu \nabla^2 \boldsymbol{u}. \tag{2.6}$$

The kinematic viscosity of the fluid is determined using the equation $\nu = c_s^2(\tau - 0.5)\Delta t$. For simplicity, both the lattice grid and time step are fixed at 1 in this work, that is, $\Delta x = \Delta t = 1$, as commonly observed in lattice Boltzmann simulations.

2.2. *Squirmer model*

The squirmer model as proposed by Blake (1971*b*) was adopted to simulate the motions of self-propelled particles. According to Blake (1971*b*), the prescribed slip velocity at a squirmer's surface can be expressed as an infinite series expansion of the radial and polar components, as follows:

$$\boldsymbol{u}^S(\boldsymbol{r}) = \sum_{n=0}^{\infty} A_n \cos(n\theta)\hat{\boldsymbol{r}} + \sum_{n=1}^{\infty} B_n \sin(n\theta)\hat{\boldsymbol{\theta}}. \tag{2.7}$$

Here, $\hat{\boldsymbol{r}}$ and $\hat{\boldsymbol{\theta}}$ refer to the radial and polar unit vectors for a given point on a squirmer's surface, respectively, as shown in figure 1, and A_n and B_n are the corresponding time-dependent amplitudes. For simplicity, the radial component is usually ignored in problems associated with the locomotion of squirmers (Blake 1971*a*,*b*). Based on the same assumption, we considered the simplified squirmer model represented by the second-order

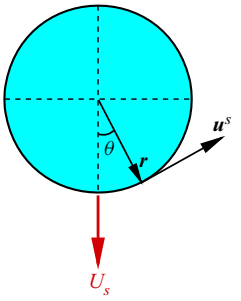

Figure 1. Schematic diagram of a circular squirmer heading downward.

truncated tangential velocity, as follows:

$$\boldsymbol{u}^S(\theta) = (B_1 \sin\theta + B_2 \sin\theta \cos\theta)\hat{\boldsymbol{\theta}}. \tag{2.8}$$

In the above, the coefficient B_1 contributes to the propulsion of the squirmer, thereby determining the steady-state swimming velocity $U_s = B_1/2$ at the Stokes flow limit. In contrast, the coefficient B_2 determines the vorticity intensity around the squirmer. Accordingly, a key parameter, defined as $\beta = B_2/B_1$, is usually introduced to represent the three types of squirmers: pushers ($\beta < 0$), pullers ($\beta > 0$) and neutral squirmers ($\beta = 0$). As indicated by the type names, pushers (e.g. bacteria such as *E. coli* and *B. subtilis*) gain thrust from their rear ends. In contrast, pullers (e.g. algae, such as *C. reinhardti*) gain thrust from their front ends (Koch & Subramanian 2011). Neutral squirmers (e.g. *Volvox*) are associated with symmetric flow without vorticity (Fadda *et al.* 2020). The streamline structures may provide a direct view of the propulsion mechanism for each type of squirmer, as described in § 4.2.

2.3. *Boundary conditions*

The improved bounce-back scheme proposed by Lallemand & Luo (2003) was used to impose no-slip boundary conditions on the surfaces of the squirmers. In their study, it was demonstrated that, based on an interpolation method, the improved bounce-back scheme shows second-order accuracy in lattice Boltzmann simulations compared with the classical bounce-back scheme with first-order accuracy (Lallemand & Luo 2003). The same scheme was used in our previous studies (Nie & Lin 2019, 2020; Nie, Guan & Lin 2021).

A schematic diagram for briefly introducing the scheme is shown in figure 2. As shown in the figure, the solid squares represent solid nodes located inside the solid boundary, whereas the solid circles represent the fluid nodes. The open circle denotes the boundary node where the bounce back occurs. As indicated by Lallemand & Luo (2003), a propagation action is applied to all fluid and solid nodes after the collision step. Accordingly, the distribution functions advected from solid nodes to fluid nodes must be updated depending on the exact locations of the boundary nodes; this approach differs from that of the classical scheme. To provide a better description, we consider node A as an example. As shown in figure 2, f_8 of node A is advected from a solid node (i.e. node B) during the propagation process. To update f_8, both the nearest and second nearest-neighbouring nodes along the boundary link (i.e. $\boldsymbol{e}_8$) are considered, that is, nodes B, C and D. Correspondingly, a parameter q, defined as $q = |\mathrm{AE}|/|\mathrm{AB}|$, is introduced to determine the location of the boundary node E. Then, an interpolation method can be

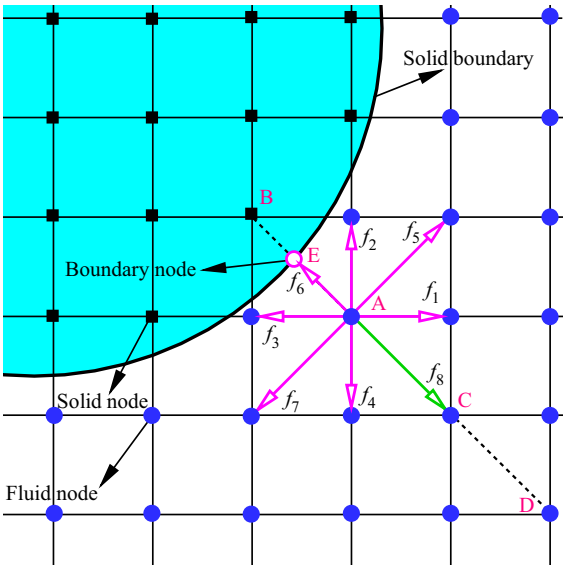

Figure 2. Schematic diagram of the improved bounce-back scheme used in this work (Lallemand & Luo 2003). Solid squares, solid nodes; solid circles, fluid nodes; open circles, boundary nodes.

employed to recompute f_8 according to the value of q

$$f_8(\mathrm{A}) = \begin{cases} q(1+2q)f_6(\mathrm{B}) + (1-4q^2)f_6(\mathrm{A}) - q(1-2q)f_6(\mathrm{C}) + 2w_8\rho\dfrac{\boldsymbol{e}_8\cdot\boldsymbol{u}_\mathrm{E}}{c_s^2} & q < \dfrac{1}{2} \\ \dfrac{1}{q(2q+1)}f_6(\mathrm{B}) + \dfrac{2q-1}{q}f_8(\mathrm{C}) - \dfrac{2q-1}{2q+1}f_8(\mathrm{D}) + \dfrac{2w_8\rho}{q(2q+1)}\dfrac{\boldsymbol{e}_8\cdot\boldsymbol{u}_\mathrm{E}}{c_s^2} & q \geq \dfrac{1}{2} \end{cases}. \tag{2.9}$$

In the above, $\boldsymbol{u}_\mathrm{E}$ is the velocity of the moving surface at boundary node E, as illustrated in figure 2. Notably, the classical bounce-back boundary is realized by (2.9) if we set $q = 0.5$. Further details on this scheme can be found in Lallemand & Luo (2003).

To account for the self-propelled motion of a squirmer, the velocity of the boundary node (e.g. node E) is updated by adding the slip velocity indicated in (2.8) before the interpolations, as follows:

$$\boldsymbol{u}_\mathrm{E} = \boldsymbol{u}_b + \boldsymbol{u}^s = \boldsymbol{U} + \boldsymbol{\Omega}\times\boldsymbol{R} + \boldsymbol{u}^S. \tag{2.10}$$

Here, $\boldsymbol{U}$ and $\boldsymbol{\Omega}$ denote the translational and rotational speeds of the squirmer, respectively, and $\boldsymbol{R}$ is the position vector from the squirmer mass centre to node E. It is inferred that the self-propelled swimming of a squirmer can only be accurately resolved if there are enough boundary nodes, suggesting that squirmers with a sufficiently large diameter are needed in the simulations.

By scanning every fluid–solid boundary link, the force and torque exerted on a squirmer can be computed using a momentum exchange scheme (Mei *et al.* 2002; Lallemand & Luo 2003). In addition, to account for the effects of covered or uncovered fluid nodes as a squirmer moves in a fluid, the method proposed by Aidun, Lu & Ding (1998) can be used to calculate the added force and torque. Accordingly, the motion of a squirmer is determined by solving Newton's equations using the net force and torque.

2.4. *Repulsive force model*

When two squirmers come close to each other, a collision may occur. To address this issue, the popular repulsive model proposed by Glowinski *et al.* (2001) was introduced, as follows:

$$\boldsymbol{F}_{ij}^{p} = \begin{cases} 0 & \text{if } S_{ij} > R_i + R_j + \xi \\ \dfrac{c_{ij}}{\varepsilon_p}\left(\dfrac{R_i + R_j + \xi - S_{ij}}{\xi}\right)^2 \dfrac{(\boldsymbol{X}_i - \boldsymbol{X}_j)}{S_{ij}} & \text{if } S_{ij} \le R_i + R_j + \xi \end{cases}. \tag{2.11a}$$

Here, R_i and R_j denote the radii of the two squirmers with mass centres at positions $\boldsymbol{X}_i$ and $\boldsymbol{X}_j$, respectively, S_{ij} is the distance between the mass centres, i.e. $S_{ij} = |\boldsymbol{X}_i - \boldsymbol{X}_j|$, and ξ represents the cutoff distance below which the repulsive force takes effect, which was set to be $1.5\Delta x$, where ε_p is a given positive stiffness parameter chosen to separate the two squirmers. As noted by Glowinski *et al.* (2001), c_{ij} serves as a force scaling factor, and is defined as the difference between the gravitational and buoyancy forces of the squirmer in the simulations. A squirmer–wall collision is treated in a similar manner, as follows:

$$\boldsymbol{F}_{ij}^{w} = \begin{cases} 0 & \text{if } S'_{ij} > R_i + R_j + \xi \\ \dfrac{c_{ij}}{\varepsilon_w}\left(\dfrac{R_i + R_j + \xi - S'_{ij}}{\xi}\right)^2 \dfrac{(\boldsymbol{X}_i - \boldsymbol{X}'_j)}{S'_{ij}} & \text{if } S'_{ij} \le R_i + R_j + \xi \end{cases}. \tag{2.11b}$$

In the above, $\boldsymbol{X}'_j$ is the position of the nearest imaginary squirmer's mass centre located on a wall, and accordingly, $S'_{ij} = |\boldsymbol{X}_i - \boldsymbol{X}'_j|$; ε_w is similar to ε_p, and is used for squirmer–wall collisions. In this study, both ε_p and ε_w were fixed at 10^{-3} in the simulations. This choice had little influence on the motions of the squirmers, as discussed in § 5.2.

To check the influence of collision strategy, another repulsive force model (Ishikawa *et al.* 2007; Ishikawa, Locsei & Pedley 2008) was also introduced, which is in exponential form as follows:

$$\boldsymbol{F}_{ij}^{p} = \begin{cases} 0 & \text{if } S_{ij} > R_i + R_j + \xi \\ \alpha_1 \dfrac{\alpha_2 \exp[-\alpha_2(S_{ij} - R_i - R_j)/R_i]}{1 - \exp[-\alpha_2(S_{ij} - R_i - R_j)/R_i]} \dfrac{(\boldsymbol{X}_i - \boldsymbol{X}_j)}{S_{ij}} & \text{if } S_{ij} \le R_i + R_j + \xi \end{cases}, \tag{2.12}$$

where α_1 is a dimensional coefficient and α_2 is a dimensionless coefficient.

3. Problem

As illustrated in figure 3, we simulated the motion and interactions of the two squirmers under gravity in a vertical channel of a width L filled with a fluid with a density ρ and viscosity ν. The density and diameter of the squirmers are denoted by ρ_s and d, respectively. We use X and Y to characterize the horizontal and vertical positions, respectively. The orientation (or swimming direction) of the squirmer is denoted by ϕ. Moreover, the subscripts indexed by '1' and '2' are used to represent the lower (squirmer 1) and upper (squirmer 2) squirmers in the initial arrangement shown in figure 3, respectively. A moving computational domain was used to simulate an infinite channel. Doing this shifts the fluid field and squirmer positions up by one lattice spacing once the lower squirmer falls below a height of H_u from the bottom boundary. This ensures that the top boundary is

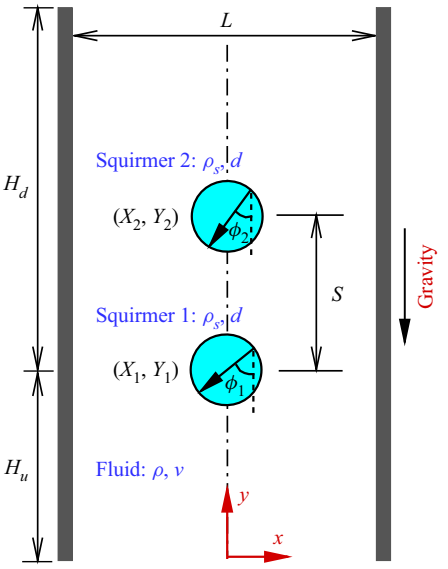

Figure 3. Schematic diagram of the problem and some notations used herein. The initial settings are as follows unless otherwise stated: $X_1(0) = X_2(0) = 0$, $Y_1(0) = 10d$, $Y_2(0) = 12d$, $\phi_1(0) = \phi_2(0) = 0$. The channel width is $L = 5d$, and the lower squirmer (squirmer 1) is initially located at a height away from the bottom boundary $H_u = 10d$ and from the top boundary $H_d = 30d$. This results in a $5d \times 40d$ computational domain.

always H_d away from the lower squirmer, leading to $H = H_u + H_d$. The normal derivative of the velocity is zero at the top boundary, and the velocity at the bottom boundary is zero.

For most of the cases studied in this work, the squirmers were initially placed at the channel centreline with a centre-to-centre distance of $S\,(0) = 2d$, as indicated in figure 3. Although the symmetrical in-line arrangement is simple, it rules out other factors to the greatest extent, suggesting that we can directly check the interactions (e.g. attraction or repulsion) between different types of squirmers. The influence of the initial arrangement is examined in § 5.2.

To account for the self-propelling strength of the squirmers in a gravitational field, a key control parameter is introduced as follows:

$$\alpha = \frac{U_s}{U_g}. \tag{3.1}$$

In the above, $U_s = B_1/2$, and U_g represents the sedimentation velocity of a non-squirmer particle settling under gravity in a channel. Notably, a Stokes-like sedimentation velocity is usually achieved for a three-dimensional study at low Reynolds numbers, based on the assumption that the gravitational and buoyancy forces are balanced by the Stokes drag for a spherical particle settling in an unbounded medium. However, there is no Stokes solution for a two-dimensional analysis. To address this issue, we adopted the analytical formula established by Happel & Brenner (1965) to determine the sedimentation velocity U_g. The formula accounts for the drag of a circular cylinder of diameter d settling in a two-dimensional channel of width L at low Reynolds numbers, as follows:

$$F_d = 4\pi K \mu U_g. \tag{3.2}$$

Here, $\mu = \rho\nu$, and K is a coefficient associated with the inverse of the blockage ratio (i.e. $\gamma = L/d$); K is defined as follows (Happel & Brenner 1965):

$$K = \frac{1}{\ln\gamma - 0.9157 + 1.7244/\gamma^2 - 1.7302/\gamma^4 + 2.4056/\gamma^6 - 4.5913/\gamma^8}. \tag{3.3}$$

When the drag is balanced by the gravitational and buoyancy forces, the sedimentation velocity of a circular cylinder can be expressed as follows:

$$U_g = \frac{d^2}{16K\mu}(\rho_s - \rho)g. \tag{3.4}$$

Accordingly, we can vary the value of α to adjust the strength of the self-propulsion with respect to the effect of gravity. Meanwhile, based on U_g or U_s, the corresponding Reynolds number can be defined as follows:

$$Re_g = \frac{\rho U_g d}{\mu}, \tag{3.5a}$$

$$Re_s = \frac{\rho U_s d}{\mu}. \tag{3.5b}$$

Certain parameters in the simulations were fixed as follows, unless otherwise specified: $L = 5d$ (corresponding to $\gamma = 5$), $H_u = 10d$, $H_d = 30d$ (resulting in $H = 40d$), $\rho = 1$, $\rho_s = 1.01$, $d = 40$ and $Re_g = 0.5$. The initial positions of the squirmers were set as follows: $X_1(0) = X_2(0) = 0$, $Y_1(0) = 10d$ and $Y_2(0) = 12d$. The swimming directions of both squirmers were initially downward, i.e. $\phi_1(0) = \phi_2(0) = 0$.

4. Validation

The present LBM was previously validated in our two-dimensional (Nie & Lin 2019; Nie *et al.* 2021) and three-dimensional (Nie & Lin 2020) studies. To add credibility, the relationship for the drag of a circular cylinder (3.2) is confirmed in § 4.1. We provide a validation for the squirmer model (Blake 1971*b*) in § 4.2.

4.1. *Sedimentation of a non-squirmer particle in a vertical channel*

Figure 4 shows the terminal velocity of a (circular) non-squirmer particle settling under gravity in a $5d$ channel as a function of Re_g. The terminal velocity is normalized by the theoretical velocity indicated by (3.4), i.e. $|U_T^*| = |U_T|/U_g$. Equation (3.4) accurately predicts the sedimentation velocity of a non-squirmer particle in a channel with a negligible fluid inertia (i.e. $Re_g < 1$), validating the effectiveness of (3.2). Figure 4 also shows that, as Re_g increases, (3.4) begins to overpredict the terminal velocity, i.e. $|U_T^*| < 1$. The reason for this is that the linear relationship between the drag of a particle and its velocity, as indicated by (3.2), no longer holds when the fluid inertia becomes significant.

4.2. *Free-swimming motion of a single squirmer in an unconfined domain*

To validate the squirmer model used in this study (2.8), we simulated the free-swimming motion of a single squirmer in a $20d \times 20d$ square domain with periodic boundary conditions in all directions. Two sets of Reynolds numbers were considered: $Re_s = 0.01$ and $Re_s = 0.5$. The swimming velocity of the squirmer was normalized to U_s, as shown in figure 5. As shown, the pusher is represented by $\beta = -5$, whereas the puller is represented

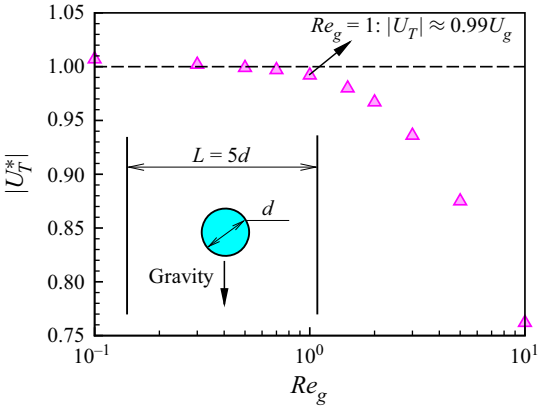

Figure 4. Normalized terminal velocity of a non-squirmer particle (i.e. $|U_T^*| = |U_T|/U_g$) settling under gravity in a $5d$ channel as a function of Re_g. Note that $|U_T^*| \approx 0.99$ at $Re_g = 1$.

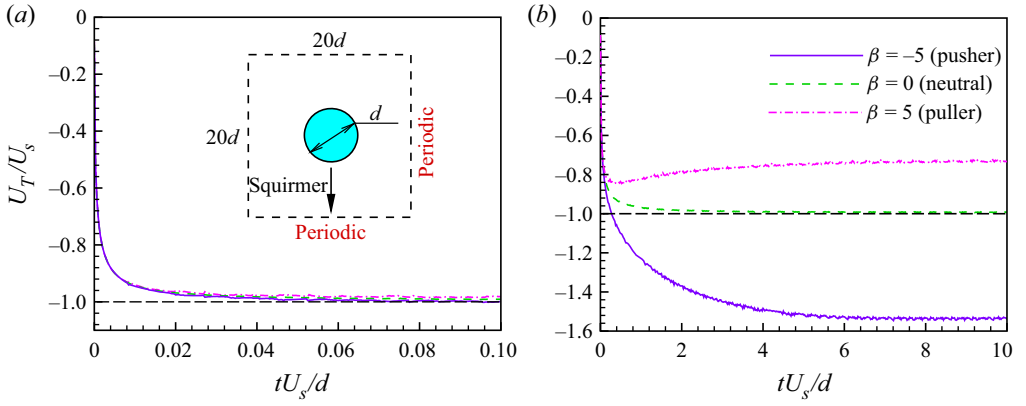

Figure 5. Time history of the normalized terminal velocities (U_T/U_s) of free-swimming squirmers in a $20d \times 20d$ square domain with periodic boundary conditions in all directions for (*a*) $Re_s = 0.01$ and (*b*) $Re_s = 0.5$, respectively. The width of the square domain is $20d$.

by $\beta = 5$. It is clearly seen that the theoretical swimming velocity is achieved for each type of squirmer at $Re_s = 0.01$ (figure 5*a*). In addition, there is no visible difference in the time evolution of U_T for all of the studied squirmers. Figure 6 (top row) shows the streamline structures around each squirmer for the same Reynolds number. The upward streamlines behind the pusher are generated by the 'push' action of the pusher from its rear end, as shown in figure 6 (*a*, top row). Accordingly, the downward swimming motion of the pusher generates downward streamlines ahead. The opposite behaviour is observed for the puller, as shown in figure 6 (*c*, top row). In contrast, figure 6 (*b*, top row) shows the streamlined structure around a neutral squirmer; it is similar to that of a non-squirmer particle. Our results agree well with those of previous studies (Ouyang *et al.* 2018; Shen, Würger & Lintuvuori 2018), confirming that the present computation method combined with the choice of $d = 40$ can accurately resolve the swimming motions of squirmers.

The situation is different at low but finite fluid inertia (e.g. $Re_s = 0.5$), as shown in figure 5(*b*). The pusher obtains a swimming velocity larger than U_s($U_T \approx 1.5U_s$), whereas the puller obtains a smaller swimming velocity ($U_T \approx 0.7U_s$). In contrast, the neutral

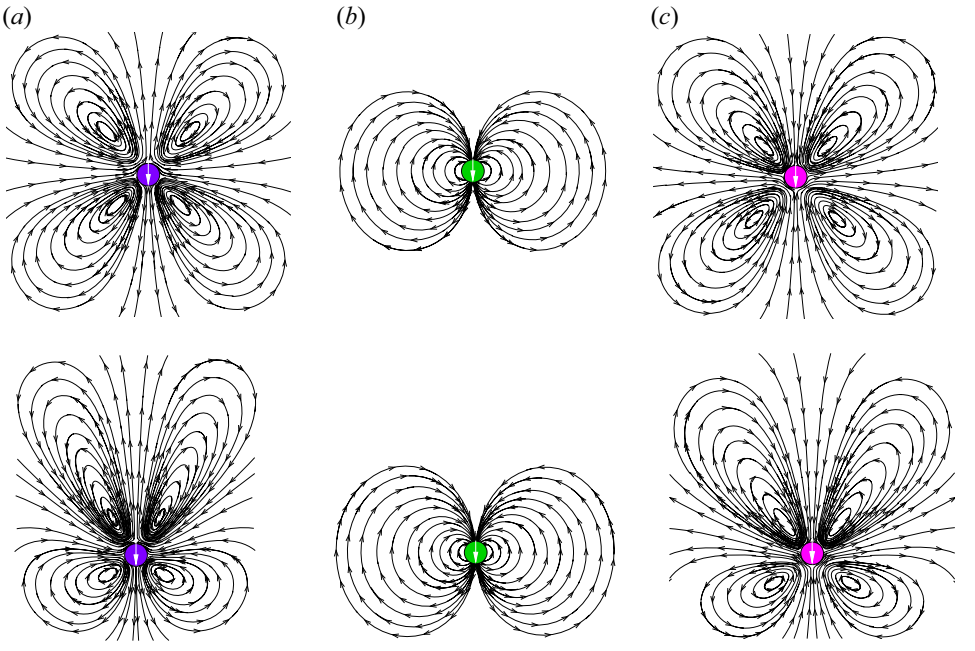

Figure 6. Streamlines around the squirmer at $Re_s = 0.01$ (top row) and $Re_s = 0.5$ (bottom row), respectively, for: (*a*) $\beta = -5$ (a pusher), (*b*) $\beta = 0$ (a neutral squirmer) and (*c*) $\beta = 5$ (a puller). Note that the arrow on each squirmer denotes its squirming axis or swimming direction (the same as below).

squirmer still swims at the theoretical speed at this Reynolds number. One possible mechanism for these results is discussed in § 5.1. Note that the observations shown in figure 5(*b*) are qualitatively consistent with those from previous numerical studies (Lin & Gao 2019) and theoretical predictions (Khair & Chisholm 2014) for a spherical squirmer freely swimming at low but finite Reynolds numbers. The corresponding streamlines are shown in figure 6 (bottom row). It can be seen that, for both the pusher and puller, the recirculation regions upstream are suppressed whereas those downstream are stretched (owing to the higher swimming speed). However, no visible difference in the streamline structures is observed for the neutral squirmer when $Re_s = 0.5$.

5. Results

The simulation results and discussion are provided in this section. To better illustrate the interactions between two squirmers in a channel, an overview of the motion of a single squirmer settling in a channel is presented in § 5.1. The interactions between the pullers or pushers in the channel are examined in §§ 5.2 and 5.3, respectively. In particular, we describe how a puller interacts with a pusher with different initial arrangements in § 5.4. For all studied cases, the self-propelling strength factor ranges between 0.4 and 1.2, i.e. $0.4 \leq \alpha \leq 1.2$, and the squirmer-type factor falls within $[-5, 5]$, i.e. $-5 \leq \beta \leq 5$. The results for small but non-zero α (e.g. $0 < \alpha < 0.4$) are not included in this study, because gravity nearly dominates the motions of squirmers when α is small. This is beyond our concern. However, the special case of $\alpha = 0$, corresponding to the case of non-squirmer particles, is included for the purpose of comparison.

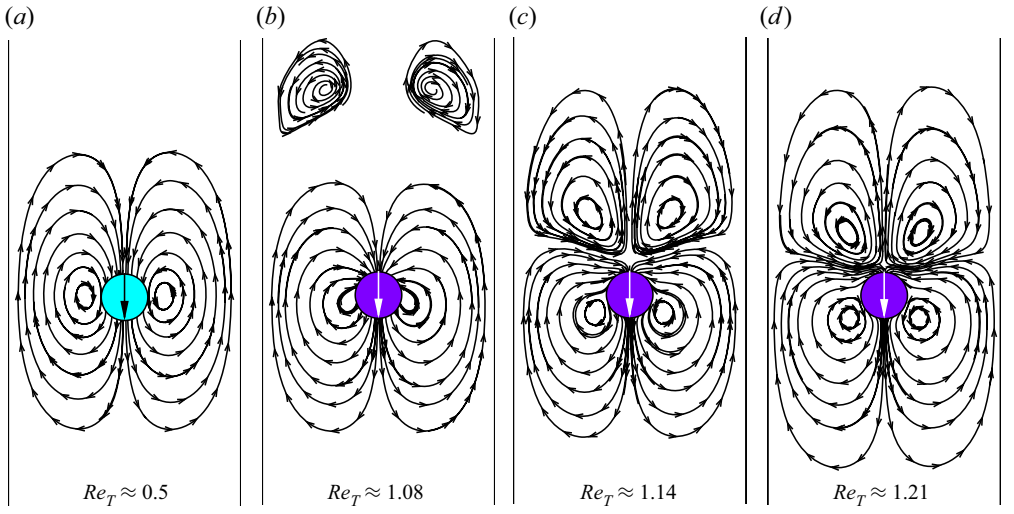

Figure 7. Instantaneous streamlines around a non-squirmer particle or squirmer settling in the channel, showing states of SDF for all cases: (*a*) $\alpha = 0$ (non-squirmer), (*b*) $\beta = -1$ ($\alpha = 1.2$), (*c*) $\beta = -3$ ($\alpha = 1.2$) and (*d*) $\beta = -5$ ($\alpha = 1.2$). Each result was obtained when the particle/squirmer reaches its steady state. Also shown in each panel is the terminal Reynolds number (Re_T), which is based on the terminal velocity of the particle or squirmer. Note that the 'trailing negative flow' is seen behind the pusher, as shown in (*b–d*).

5.1. *Overview of the sedimentation of a single squirmer in a channel*

Figure 7 shows the instantaneous streamlines around a pusher ($\beta = -1$, -3 or -5) at a steady state at $\alpha = 1.2$. The results for a non-squirmer particle are shown in figure 7(*a*). All cases in figure 7 exhibit a similar pattern, referred to as the 'steady downward falling' (SDF) pattern in this work. The most significant feature characterizing the flow around a pusher may be the 'trailing negative flow' behind it, as seen in figure 7(*b–d*). The 'trailing negative flow' exhibits an opposite direction as the pusher moves downward, becoming stronger and getting closer to the pusher with increasing $|\beta|$. The terminal Reynolds number (Re_T) based on the terminal velocity U_T is also indicated for each case in figure 8. It is clear that the U_T of the pushers is more than twice that of the non-squirmer particle. In addition, the U_T is larger for a pusher with a larger $|\beta|$ when the self-propelling strength factor remains the same (i.e. $\alpha = 1.2$); this is associated with the 'trailing negative flow'. The stronger the 'trailing negative flow', the larger the reversed thrust the pusher experiences.

For the settling of a single puller ($\beta > 0$), the situation is quite different. Figures 8 and 9 show the instantaneous streamlines around a puller ($\beta = 1$, 3 and 5) at $\alpha = 0.6$ and 1.2, respectively. The case of a neutral squirmer is also included for comparison (figures 8*a* and 9*a*). The puller exhibits a steady state of falling downward at $\beta = 5$ for both values of α (figures 8*d* and 9*d*), similar to the behaviour of a pusher (figure 7). However, in this case, the 'negative flow' leads the puller. The puller gains a reversed thrust owing to the 'leading negative flow', resulting in a decrease in its terminal velocity (as demonstrated by the terminal Reynolds numbers indicated in figures 8*a* and 8*d* or 9*a* and 9*d*). No 'negative flow' is observed for the neutral squirmer (figures 8*a* and 9*a*). This also explains why the puller and pusher reach different swimming velocities at a higher Re_s, as shown in figure 5(*b*).

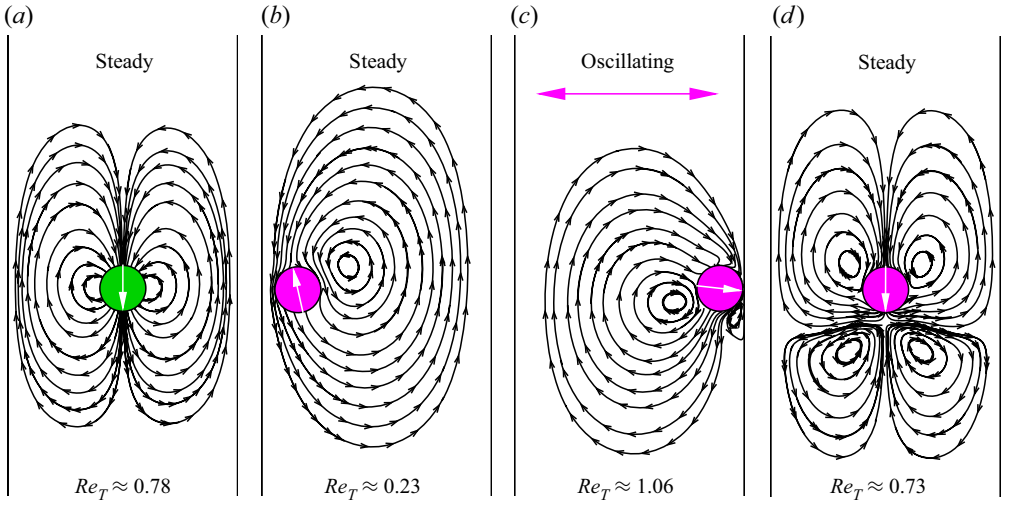

Figure 8. Instantaneous streamlines around a squirmer settling in the channel at $\alpha = 0.6$ for (*a*) $\beta = 0$ (SDF), (*b*) $\beta = 1$ (SIF), (*c*) $\beta = 3$ (LSO) and (*d*) $\beta = 5$ (SDF). For $\beta = 3$, the result when the puller reaches its rightmost position was chosen. Note that the 'leading negative flow' is seen ahead of the puller for $\beta = 5$, as shown in (*d*).

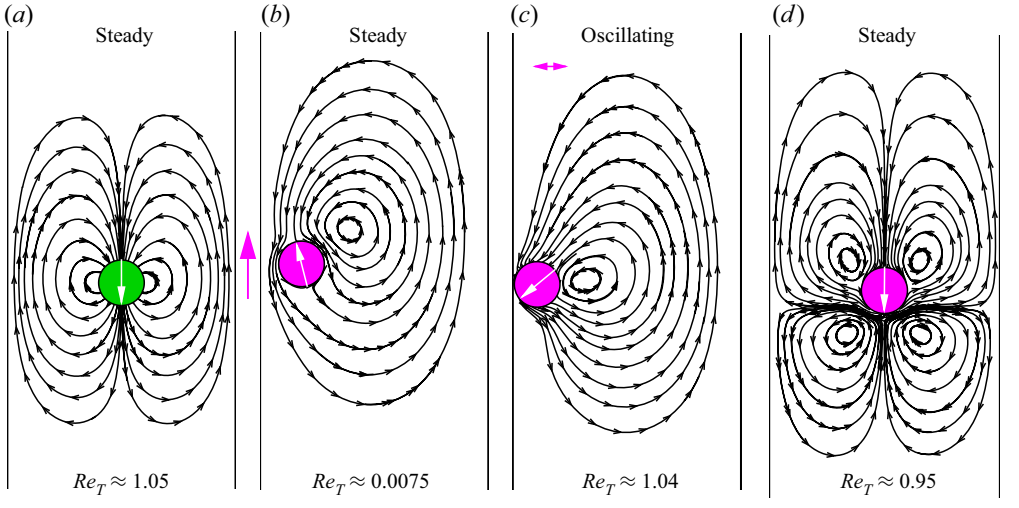

Figure 9. Instantaneous streamlines around a squirmer at $\alpha = 1.2$ for (*a*) $\beta = 0$ (SDF), (*b*) $\beta = 1$ (SIR), (*c*) $\beta = 3$ (SSO) and (*d*) $\beta = 5$ (SDF). For $\beta = 3$, the result when the puller reaches its leftmost position was chosen. Note that the upward arrow in (*b*) indicates that the squirmer eventually rises (the same as below). The 'leading negative flow' is seen ahead of the puller for $\beta = 5$, as shown in (*d*).

In contrast, at $\beta = 1$, the puller ultimately reaches a steady state of inclined falling ($\alpha = 0.6$, figure 8*b*) or inclined rising ($\alpha = 1.2$, figure 9*b*), with its orientation upward. These patterns are referred to as 'steady inclined falling' (SIF) and 'steady inclined rising' (SIR), respectively. One possible reason for these inclined patterns is provided below. In particular, no steady state is achieved at $\beta = 3$ for the puller, which instead undergoes a periodic motion in the channel with a large scale ($\alpha = 0.6$, figure 8*c*) or that with

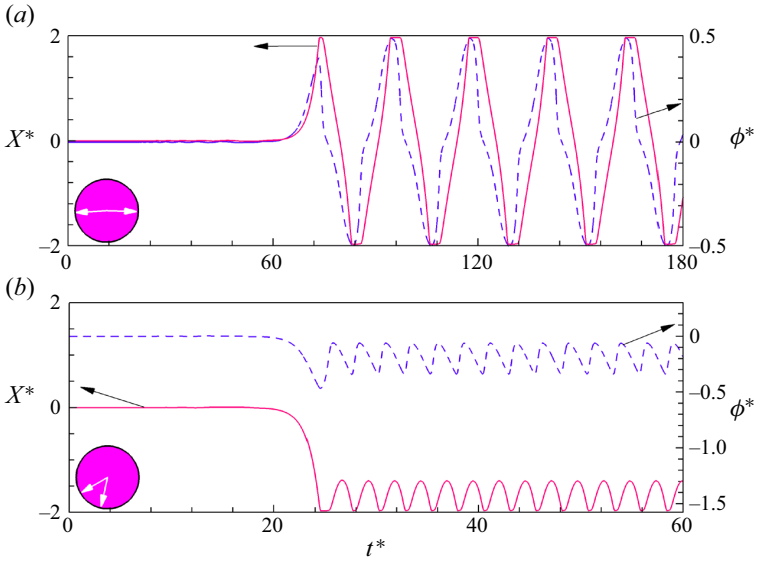

Figure 10. Time history of the horizontal position as well as the orientation of a puller ($\beta = 3$) at (*a*) $\alpha = 0.6$ and (*b*) $\alpha = 1.2$, illustrating the LSO and SSO patterns, respectively. Note that the horizontal position and orientation of squirmers are normalized through $X^* = X/d$ and $\phi^* = \phi/\pi$ (the same as below).

small scale ($\alpha = 1.2$, figure 9*c*), designated here as 'large-scale oscillating' (LSO) and 'small-scale oscillating' (SSO) patterns, respectively. The SSO pattern was reported and referred to as the 'attracted oscillatory mode' in a previous study (Ouyang & Lin 2022).

To better illustrate the LSO and SSO patterns, figure 10 shows the time series of the puller's horizontal position ($X^* = X/d$) and orientation ($\phi^* = \phi/\pi$) at $\beta = 3$ for $\alpha = 0.6$ and $\alpha = 1.2$, respectively. It is observed that for $\alpha = 0.6$, the puller moves from one channel wall ($X^* = -2$) to the other ($X^* = 2$), with its orientation varying approximately from $-\pi/2$ to $\pi/2$ (figure 10*a*). Therefore, the pattern of the LSO is characterized by a large variation in its displacement, as well as a large variation in its orientation. In contrast, figure 10(*b*) shows the SSO pattern with a puller oscillating around a line close to a channel wall (i.e. $X^* = -2$), with small amplitudes in both its displacement and orientation.

It seems that pullers ($\beta > 0$) are more likely to lose their stability than pushers ($\beta < 0$) or neutral squirmers ($\beta = 0$) under the same conditions (see figures 7–9). Regarding the issue, we show the pressure contours around squirmers of different types ($\beta = -5$, 0, and 5) at $\alpha = 1.2$ in figure 11. For these cases, the same state (SDF) is ultimately realized. As shown in figure 11(*b*), the pressure distribution of the neutral squirmer is similar to that of a non-squirmer particle (not shown here), with high-pressure and low-pressure regions observed before and behind it, respectively. For the pusher, however, significant high-pressure regions are seen both before and behind it, whereas low-pressure regions are located at both lateral sides of the pusher (figure 11*a*). Accordingly, the pressure distribution around the puller exhibits the opposite trend (figure 11*c*). Therefore, a puller may experience large repulsive forces exerted on its lateral sides as it settles downward in a channel, resulting in an unstable situation. Once the symmetrical configuration of a puller is broken, it may change into a state of SIF (figure 8*b*), SIR (figure 9*b*), LSO (figure 8*c*) or SSO (figure 9*c*). This usually occurs at a small or intermediate β value for the puller. However, at a large value of β, the wall-repulsive effects become strong, owing to the significant high-pressure regions. This suppresses the puller from deviating from the

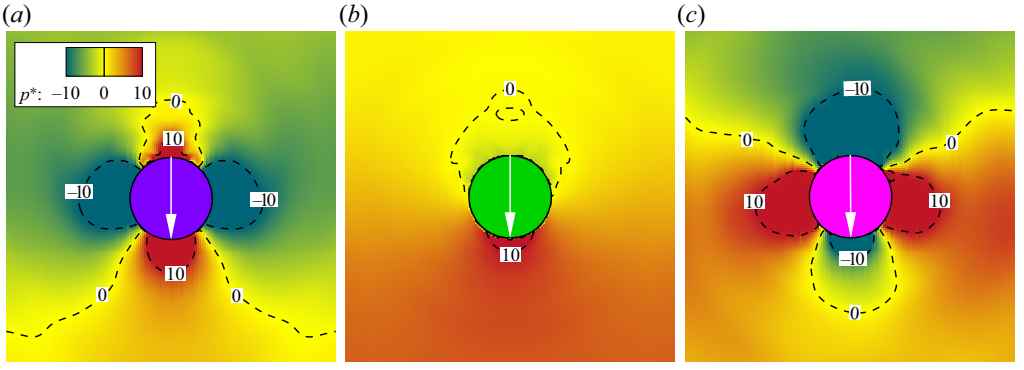

Figure 11. Instantaneous pressure distribution around a squirmer showing the SDF pattern at $\alpha = 1.2$: (*a*) $\beta = -5$, (*b*) $\beta = 0$ and (*c*) $\beta = 5$. Note that the pressure is normalized through $p^* = (p - p_\infty)/(\rho U_T^2)$, where p_∞ represents the pressure of the undisturbed flow.

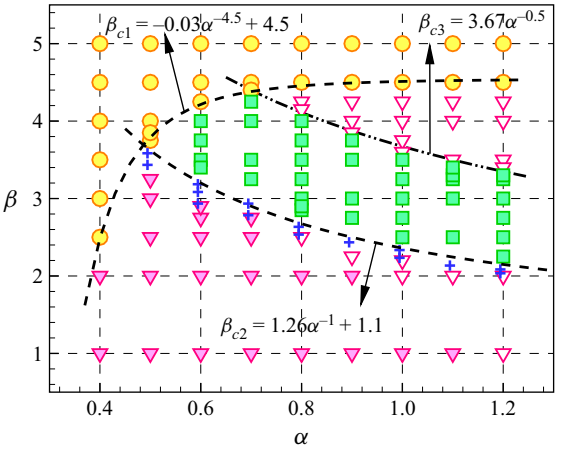

Figure 12. Summarization of the patterns of motion for a puller settling in the channel in the parametric space (α, β). Each pattern of motion is characterized by one symbol (the same as below). Circle, SDF; plus, LSO; square, SSO; filled gradient, SIF; open gradient, SIR. Note that the boundaries between regions of different patterns (i.e. β_{c1}, β_{c2} and β_{c3}) were obtained through the least-square scheme.

channel centreline in the presence of a flow disturbance (figures 8*d* and 9*d*). In addition, we can predict from figure 11 that two pushers attract each other when in a side-by-side arrangement, whereas two pullers repel each other. This is consistent with the findings of Götze & Gompper (2010), who simulated the motion of a pair of squirmers using MPCD. To address the motion of a single puller more clearly, we conducted extensive simulations and summarized the patterns in the parametric space (α, β), as shown in figure 12.

As shown in figure 12, five patterns are revealed according to both self-propelling strength (α) and squirmer type factor (β): SDF, LSO, SSO, SIF and SIR. Three boundary limits (indicated by β_{c1}, β_{c2} and β_{c3}) were obtained through the least-squares scheme based on the boundary data between regions of different patterns. For $\beta \geq \beta_{c1}$, the puller maintains its initial symmetrical configuration, and exhibits the SDF pattern of regardless of α. On the opposite side, it is widely observed that the puller loses its stability at the channel centreline before it regains it somewhere close to the channel walls when undergoing the SIF or SIR pattern, depending on both α and β.

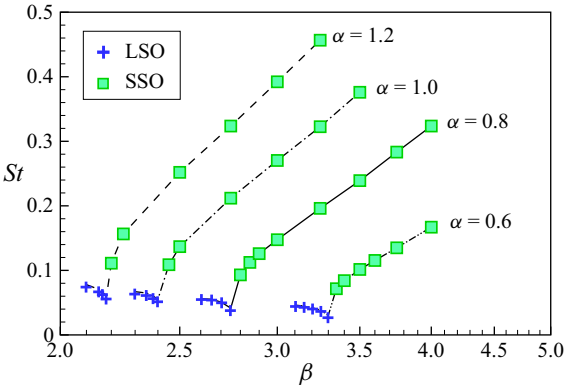

Figure 13. Dimensionless oscillating frequencies (Strouhal number, i.e. $St = f^*d/U_g$ where f is the frequency) of a puller undergoing an LSO or SSO motion. The symbols (plus, LSO; square, SSO) are identical to those used in figure 13.

Moreover, figure 12 shows the SSO pattern for the puller at intermediate values of β ($\beta_{c2} < \beta < \beta_{c3}$). In particular, it is rare to find the LSO pattern for a puller, which occurs in a very narrow range of β approximately centred at β_{c2}, as shown in figure 12. Notably, no LSO-like pattern was reported for a puller in a $2d$ channel (Ouyang & Lin 2022). In addition, the two oscillating patterns differ not only in their amplitudes but also in their frequencies, as shown in figure 13. This provides a comparison of the dimensionless frequency (Strouhal number, St) for the SSO and LSO patterns. It can be observed that St is much smaller for the LSO pattern than for the SSO pattern. Furthermore, the oscillating frequency exhibits opposite trends with increasing β for the two patterns (figure 13).

As stated above, the pusher ($\beta < 0$) maintains its initial symmetrical configuration and exhibits the SDF pattern for all values of α and β studied here in the initial downward orientation, i.e. $\phi^*(0) = 0$. To provide references for the study of the interactions between squirmers, we conducted extra simulations for a pusher at another initial orientation, i.e. $\phi^*(0) = 0.1$. The patterns are summarized in figure 14. Five similar patterns are revealed for the pushers, which are represented by the same symbols used in figure 12. Figure 14 indicates that the SDF pattern only exists at a large $|\beta|$ for the pusher, similar to the case of a puller. In contrast, for almost every β falling within $[-4, -2]$, the pusher undergoes LSO or SSO motions, depending primarily on β. However, the inclined patterns (SIF and SIR) are only observed at $\beta = -1$. Notably, the present LSO is similar to the 'oscillatory mode' for pushers reported by Ouyang & Lin (2022). Ahana & Thampi (2019) also revealed that weak pushers (small $|\beta|$) confined in a channel may undergo an oscillatory trajectory spanning the channel width. This type of swimming pattern can potentially be used to enhance the mixing of suspensions in microfluidic channels at low Reynolds numbers (Najafi, Raad & Yousefi 2013; Jalali, Khoshnood & Alam 2015).

As shown in figure 14, a pusher may also form a stable inclined structure adjacent to its nearby wall, corresponding to the SIF or SIR patterns. However, a significant difference is observed between the pusher and puller, as shown in figure 15. The former has an outward orientation, whereas the latter has an inward orientation. This difference is also visible in the SSO pattern for both squirmers. To address this point, we mark all the forces experienced by each squirmer in figure 15. For the pusher, to achieve a stable structure, a self-propelling force is needed to balance the attractive force owing to the significant low-pressure regions on its left side. This requires the pusher to swim outward (figure 15*a*). Note that Berke *et al.* (2008) experimentally studied the distribution of swimming bacteria

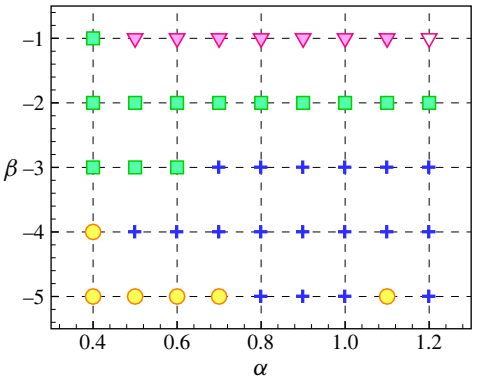

Figure 14. Summary of the pattern of a pusher's motion in the parametric space (α, β) for $\phi^*(0) = 0.1$. The same symbols as those in figure 13 are used, i.e. circle, SDF; plus, LSO; square, SSO; filled gradient, SIF; open gradient, SIR.

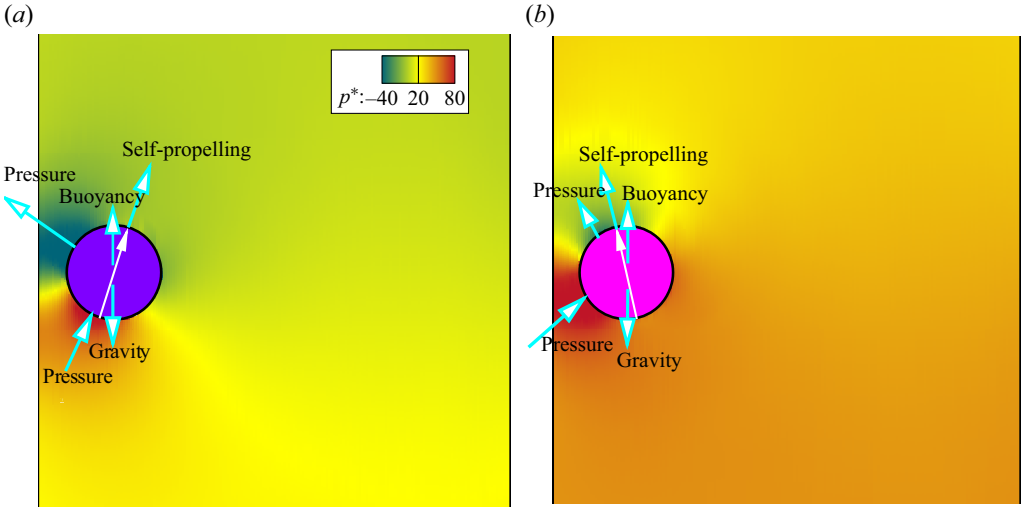

Figure 15. Instantaneous contours of normalized pressure at steady state (SIF) at $\alpha = 0.6$ for (*a*) a pusher ($\beta = -1$) and (*b*) a puller ($\beta = 1$). To illustrate the orientations of the squirmers, schematic diagrams of the forces experienced by each squirmer are also shown.

(*E. coli*) between two glass plates and found significant attraction of the bacteria by the surfaces. From a theoretical perspective, Berke *et al.* (2008) proposed that it is the hydrodynamic interactions with the walls that lead to the reorientation of the bacteria in the direction parallel to the walls and the attraction. This is qualitatively consistent with figure 15(*a*) when we consider the difference between the shapes of our pushers (circular) and the actual bacteria *E. coli* (spheroidal with lengths of approximately 2–3 μm and diameters of approximately 1 μm, as indicated by Koch & Subramanian 2011).

In contrast to the pusher, the puller needs to swim inward to ensure that its self-propelling force balances the repulsive force resulting from the high-pressure regions on its left side (figure 15*b*). For the swimming cells such as algae *Chlamydomonas* which are pullers, Berke *et al.* (2008) predicted the attraction mechanism as well: they will simply

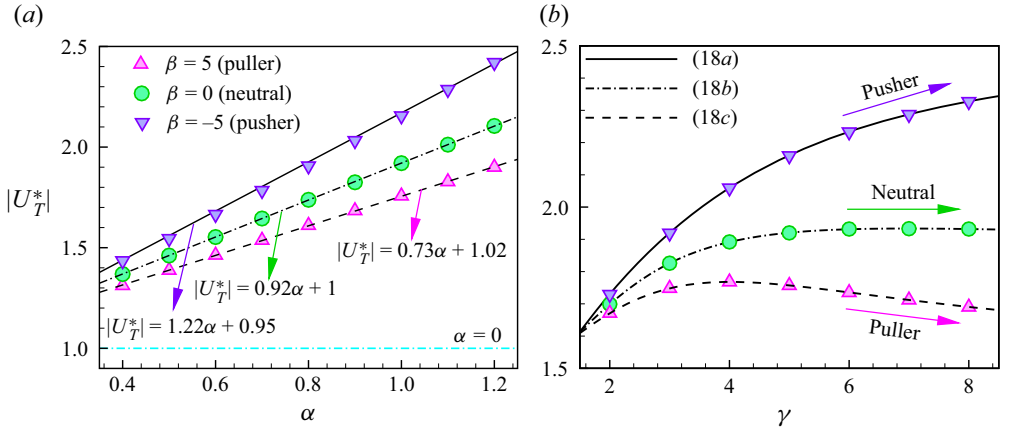

Figure 16. Terminal velocity of a squirmer ($|U_T^*| = |U_T|/U_g$, the same as below) settling in the channel as a function of (*a*) α (when γ is fixed at 5) and (*b*) the channel width (when α is fixed at 1.2). All of the fitting curves indicated in the figure were obtained through the least-square scheme.

crash into the walls. This is consistent with our observation for pullers. The low-pressure regions are located at the top and bottom of a puller (see figure 12*c*), so it may be attracted by nearby wall as it is reoriented in the direction perpendicular to the wall when the gravity-driven settling is not taken into account. This looks like that the puller crashes into its nearby wall.

Finally, we show the terminal velocities of squirmers of different types ($\beta = -5$, 0 and 5) as a function of α (when γ is fixed at 5) and the channel width (when α is fixed at 1.2) in figure 16. Notably, for all cases in the figure, the squirmer ultimately reaches the SDF state, except for $\beta = 5$ at $\gamma = 8$, for which the puller is seen to be steadily settling in the channel for a long time before changing to the SSO motion. To make a reasonable comparison, we adopted the steady velocity of the puller before the onset of the SSO for this case. It is clearly seen that the terminal velocity increases linearly with α ($0.4 \leq \alpha \leq 1.2$) for all types of squirmers, with a larger growth rate for pushers and smaller rate for pullers, as shown in figure 16(*a*). Note that the terminal velocity of the squirmers is normalized by U_g, that is, $|U_T^*| = |U_T|/U_g$. It should be stated here that for all cases considered the Reynolds numbers are so small ($Re_T < 2$) that the flow is dominated by viscous effects. This gives rise to a linear relationship between the squirmer velocity and the driving force of squirmer. For a larger α, both the 'trailing negative flow' and the 'leading negative flow' become stronger, resulting in a larger difference in the $|U_T|$ values between a puller and pusher (figure 16*a*).

In contrast, the terminal velocity shows distinct trends upon varying the channel width ($5 \leq \gamma \leq 8$) for different squirmers, as shown in figure 16(*b*). This suggests different wall effects on the motions of different types of squirmers. For the pusher, $|U_T|$ monotonically increases with γ; however, for the puller, it shows a slow decreasing trend when $\gamma > 4$. In particular, it appears that the terminal velocity remains constant when $\gamma > 4$ for a neutral squirmer. This indicates that among all types of squirmers, the pullers are the most sensitive to walls when the other conditions remain the same. Similar rational formulations, i.e. (5.1*a*)–(5.1*c*), were found to fit our simulation results excellently for all

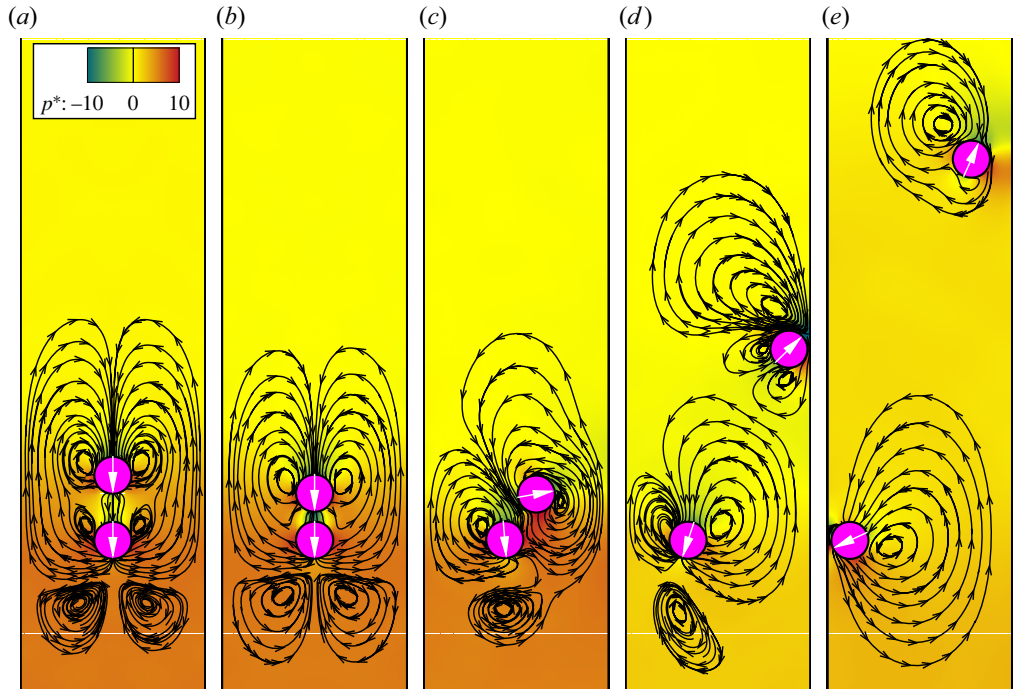

Figure 17. Instantaneous streamlines and pressure contours around two settling pullers at different times at $\beta = 2.3$ for $\alpha = 1$: (*a*) $t^* \approx 0.5$, (*b*) $t^* \approx 1$, (*c*) $t^* \approx 5$, (*d*) $t^* \approx 8$ and (*e*) $t^* \approx 11$.

squirmers (figure 16*b*)

$$|U_T^*| = (2.48\gamma^2 + 8.63\gamma + 21.66)/(\gamma^2 + 3.16\gamma + 17.92), \tag{5.1a}$$

$$|U_T^*| = (1.85\gamma^2 - 1.47\gamma + 11.27)/(\gamma^2 - 1.4\gamma + 8.04), \tag{5.1b}$$

$$|U_T^*| = (1.49\gamma^2 - 2.14\gamma + 17.42)/(\gamma^2 - 2.46\gamma + 12.36). \tag{5.1c}$$

5.2. *When a puller ($\beta > 0$) meets another puller ($\beta > 0$)*

In this section, we examine the interactions between two identical pullers settling under gravity in a $5d$ channel. Figure 17 shows the instantaneous streamlines and pressure distributions around the two settling pullers ($\beta = 2.3$) at different times for $\alpha = 1$.

It can be seen that the pullers attract each other in the initial stage, owing to the low-pressure region between them (figures 17*a* and 17*b*). After the collision, the upper puller (referred to as 'squirmer 2' in figure 3) turns its orientation upward, and is driven to move toward the right wall. The lower puller (referred to as 'squirmer 1' in figure 3), however, remains in its downward orientation, and moves toward the other wall instead (figures 17*c* and 17*d*). Owing to their opposite orientations, the pullers quickly separate from each other (figure 17*d*). Our results show that the upper puller ultimately achieves the SIR state, whereas the lower puller undergoes LSO motion.

The different behaviours of the two pullers (figure 17) are not sensitive to the collision strategy ((2.11) or (2.12)). To verify this point, we performed additional simulations for the same values of α and β while choosing different stiffness parameters, i.e. ε_p and ε_w. The trajectories of the upper puller are shown in figure 18(*a*). There are small differences between the present computations using $\varepsilon_p = \varepsilon_w = 10^{-3}$ and those obtained using 10^{-5}

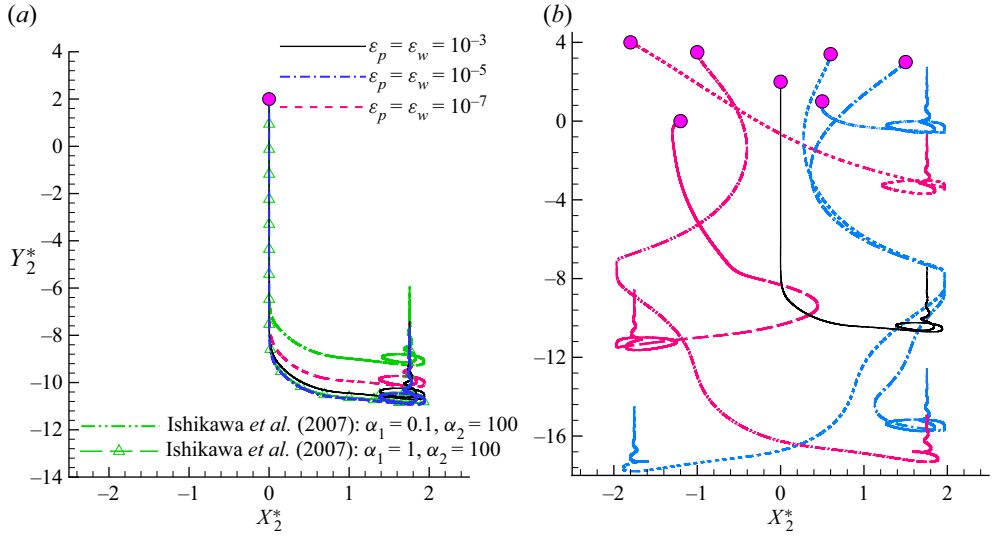

Figure 18. Effects of (*a*) collision parameter and (*b*) initial arrangement on the trajectory of the upper puller (i.e. squirmer 2 shown in figure 3). The repulsive force model (2.12) which is in exponential form was also checked in (*a*). The same α and β as those in figure 17 were chosen. The small circles represent the initial positions of the upper puller. Note that the initial position of the lower puller (referred to as 'squirmer 1' in figure 3) remains unchanged for all cases studied.

or 10^{-7}. However, the collision parameters do not change the patterns of the squirmers, as demonstrated in our previous studies (Nie & Lin 2019, 2020; Nie *et al.* 2021). This is also true when the other repulsive force model (2.12) was taken into account. Note that the model (Ishikawa *et al.* 2007, 2008) is in exponential form, completely different from the algebraic one we adopted here (Glowinski *et al.* 2001). In addition, we checked the influence of the initial arrangements by varying the initial position of the upper puller while keeping that of the lower one unchanged. Selected results are shown in figure 18(*b*), and show the same solution (SIR) as that obtained from the initial arrangement indicated in figure 3 or its symmetrical counterpart, despite the fact that the upper puller was released from various positions. Correspondingly, the lower puller undergoes an LSO motion for all settings, as indicated in figure 18(*b*). Therefore, the patterns revealed here are applicable to various initial configurations.

Our results indicate that both pullers are likely to gain a stable structure adjacent to their nearby channel walls (i.e. SIF or SIR) after they interact or collide with each other, especially at a large α. Figure 19 shows the instantaneous streamlines around two settling squirmers at steady states at different values of β for $\alpha = 1$, i.e. the same α as in figure 17. $\beta = 0$ corresponds to neutral squirmers. Both figures 17 and 19 suggest that the pullers may change their orientations noticeably when they come to contact, qualitatively in accord with previous studies (Ishikawa *et al.* 2006, 2007). The SIF pattern is seen for both squirmers at small values of β (figures 19*a* and 19*b*), whereas the SIR is seen at large values of β (figures 19*c* and 19*d*). In addition, squirmers are more inclined with respect to the channel walls at larger values of β. The reason is explained as follows. The larger the value of β , the more significant the high-pressure regions on the lateral sides of a puller (see figure 11*c*). As a result, the pullers need to be more inclined to attain a larger horizontal component of the self-propelling force to achieve a stable structure (see figure 15*b*). In particular, neutral squirmers showed no visible inclination when they

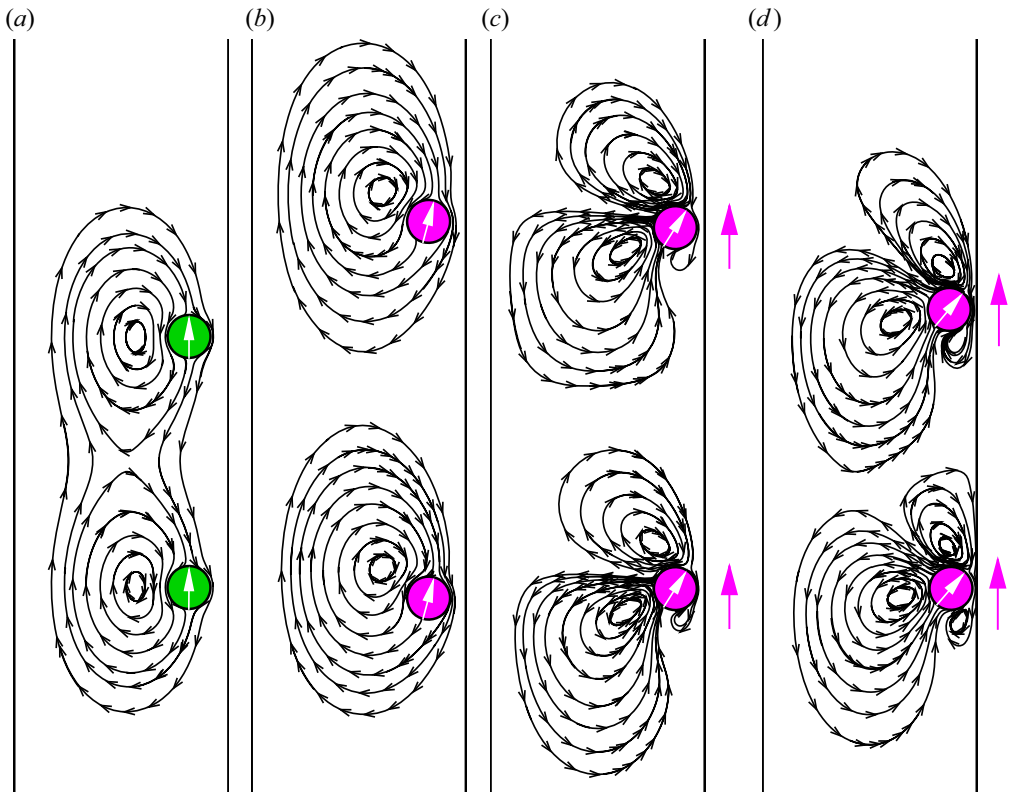

Figure 19. Instantaneous streamlines around two settling squirmers at steady state for $\alpha = 1$: (*a*) $\beta = 0$ (neutral), (*b*) $\beta = 1$, (*c*) $\beta = 3$ and (*d*) $\beta = 5$.

reach a steady state in the channel (figure 19*a*). This is reasonable, because there are no significant low-pressure or high-pressure regions on the lateral sides of a neutral squirmer, unlike in the case of a puller or pusher (see figure 11). As a result, there is no need for a neutral squirmer to incline its swimming direction to attain a stable configuration. Figure 19 also indicates that the squirmers come closer to their nearby walls at a larger β. The primary reason for this is provided below. For a puller, low-pressure regions can be seen at its front (figure 11*c*); these turn into an attractive force when the puller is inclined to its nearby wall (see also figure 15*b*). The attractive force becomes stronger at a larger β, causing the puller to move closer to the wall.

To provide greater insight into the interactions between squirmers ($\beta \geq 0$), we performed a large number of simulations. The patterns of the lower and upper squirmers are summarized in figures 20(*a*) and 20(*b*), respectively. The same symbols as those used in figure 12 are adopted except for the symbol of the cross (X), a new symbol used to represent a new pattern for which the squirmers interact with each other all the time and oscillate in the channel. Note that the oscillations are non-periodic. This new pattern is beyond the scope of this paper. It is clearly seen from figure 20 that the squirmers ($\beta \geq 0$) settle separately in the channel while exhibiting the same or different patterns for all α and β values considered, except for those indicated by X (small β at $0.4 \leq \alpha \leq 0.9$). This is significantly different from the situation in which two non-squirmer particles settle under gravity in a channel at similar Reynolds numbers. Previous studies (Feng, Hu & Joseph 1994; Nie & Lin 2019) have indicated that non-squirmer particles may form a

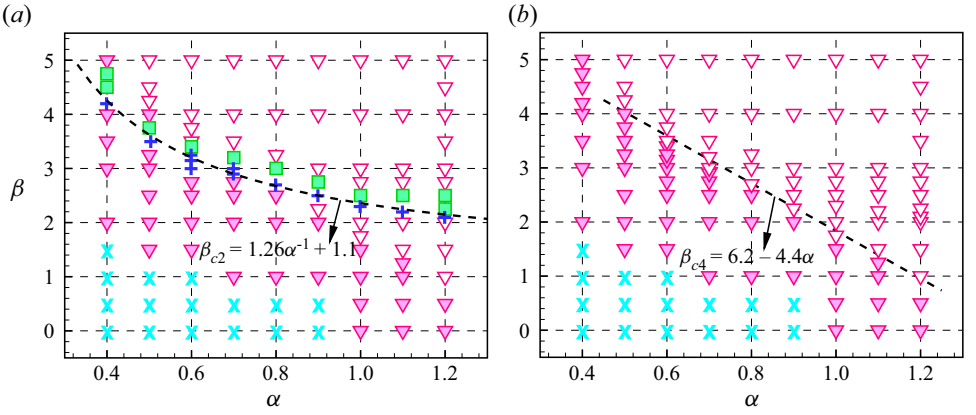

Figure 20. Summary of the patterns of two interacting squirmers ($\beta \geq 0$) in the channel in the parametric space (α, β): (a) lower squirmer (squirmer 1) and (b) upper squirmer (squirmer 2). Note that all the symbols (plus, LSO; square, SSO; filled gradient, SIF; open gradient, SIR) are identical to those in figure 12 except for a new one, i.e. the symbol of the cross '*X*', which was used here to represent a pattern of squirmers oscillating.

stable staggered configuration in which they rotate in the same direction at $Re \sim O(1)$. Further increasing the Reynolds number may lead to a periodic motion of particles or drafting–kissing–tumbling (DKT) interactions between the particles (Feng *et al.* 1994). Notably, no DKT motions are observed for any of the cases considered here.

The interactions between pullers have significant influences on the motion of both pullers as compared with figure 12 (showing the patterns of a single one). Interestingly, there is no SDF pattern for either puller (figure 20). This is primarily because the pullers always attract each other once they are released and eventually collide with each other (see also figure 17). Then, both pullers, which are initially moving downward, change their orientations, leading to patterns other than SDF. The close contact of the pullers changes their respective orientations in different manners, with the upper one always facing upward, whereas the lower one may remain downward or face upward depending on β at a certain α (figure 20). Consequently, the upper puller is always attracted by its nearby wall and reaches a steady inclined state (SIF or SIR), as shown in figure 20(*b*). The boundary between the SIF and SIR regions can be approximately formulated by a linear function related to a critical β, i.e. $\beta_{c4}(\alpha)$, as indicated in figure 20(*b*) (with its value decreasing with α). In contrast, it is the lower puller exhibits the LSO pattern for a narrow range of β; this can still be accounted for by the same formulation $\beta_{c2}(\alpha)$, as indicated in figure 12. However, the SSO pattern only exists at β values slightly larger than β_{c2}, which differs from figure 12, suggesting that the pullers are highly likely to lose stability and give rise to oscillating motions at intermediate values of β. In general, an inclined state (SIF or SIR) is largely observed for the lower puller, owing to its interactions with the upper puller.

5.3. *When a pusher ($\beta < 0$) meets another pusher ($\beta < 0$)*

Compared with the case for pullers, the interactions between two pushers are much simpler, and are in accordance with the observation of a single squirmer as discussed in § 5.1. In general, only the SDF pattern is observed for the pushers. Figure 21 shows the instantaneous streamlines and pressure contours around two pushers ($\beta = -3$) at different times for $\alpha = 1.2$. The pushers repel each other once they are released in the channel owing

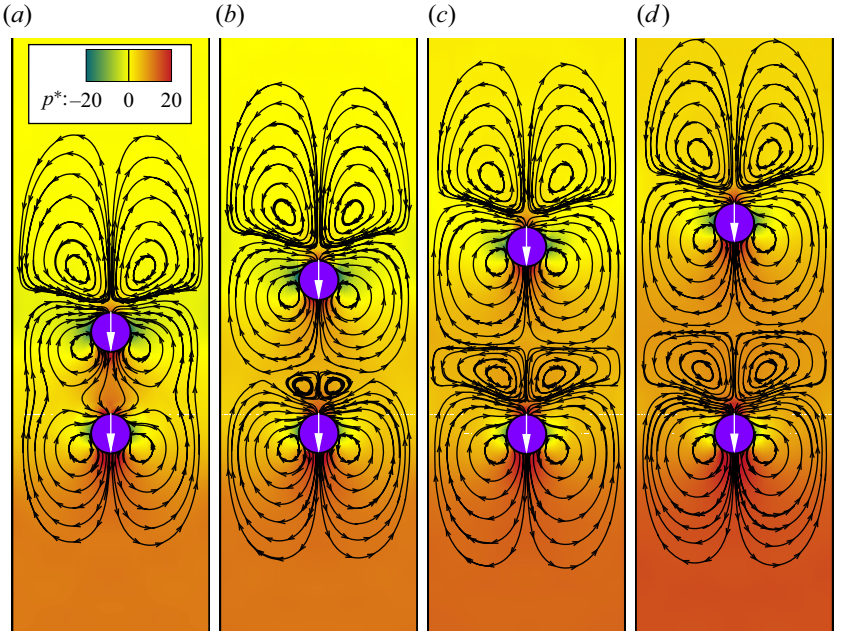

Figure 21. Instantaneous streamlines and pressure distributions around two settling pushers ($\beta = -3$) for $\alpha = 1.2$ at different times: (*a*) $t^* \approx 1$, (*b*) $t^* \approx 10$, (*c*) $t^* \approx 40$ and (*d*) $t^* \approx 100$.

to the high-pressure regions between them (figure 21*a*,*b*), which is contrary to the case with the pullers (figure 17). As the upper pusher moves farther away, the 'trailing negative flow' behind the lower pusher becomes more significant (figure 21*c*,*d*), further driving the pushers apart from each other. Figure 22 shows the instantaneous streamlines around two pushers with different β values at $t^* \approx 100$. Figure 22(*a*,*b*) suggests that the 'trailing negative flow' is not the basic reason for the repulsion of the pushers. At small values of $|\beta|$, no visible 'negative flow' is seen behind the lower pusher; it becomes visible at larger values of $|\beta|$ and helps to accelerate the separation of the pushers, as indicated in figure 22(*c*,*d*).

Our simulations show that the pushers move farther away from each other over time. In other words, the pushers will never come close to each other, owing to the high-pressure regions between them (figure 21). To address this point, we present the time history of the distances between the pushers at different values of β for both $\alpha = 0.6$ and 1.2 in figure 23. The distance is normalized by d, i.e. $S^* = S/d$. It is clearly seen that S^* increases monotonically with time for all cases considered. In particular, a similar slope is obtained at $t^* > 10$ at a large $|\beta|$ (e.g. $|\beta| \geq 3$) for either α.

5.4. *When a puller ($\beta > 0$) meets a pusher ($\beta < 0$)*

In this section, we examine the interactions between the puller and pusher. We only consider two situations: a pusher initially placed above a puller, and its opposite. For simplicity, the squirmers are assumed to have the same value of $|\beta|$. Figure 16 indicates that a pusher always moves faster in a channel than a puller if it has the same value of $|\beta|$. Accordingly, for the former situation, it is commonly observed that the pusher (say $\beta = -5$) approaches the puller (say $\beta = 5$) once they are released from rest, and ultimately,

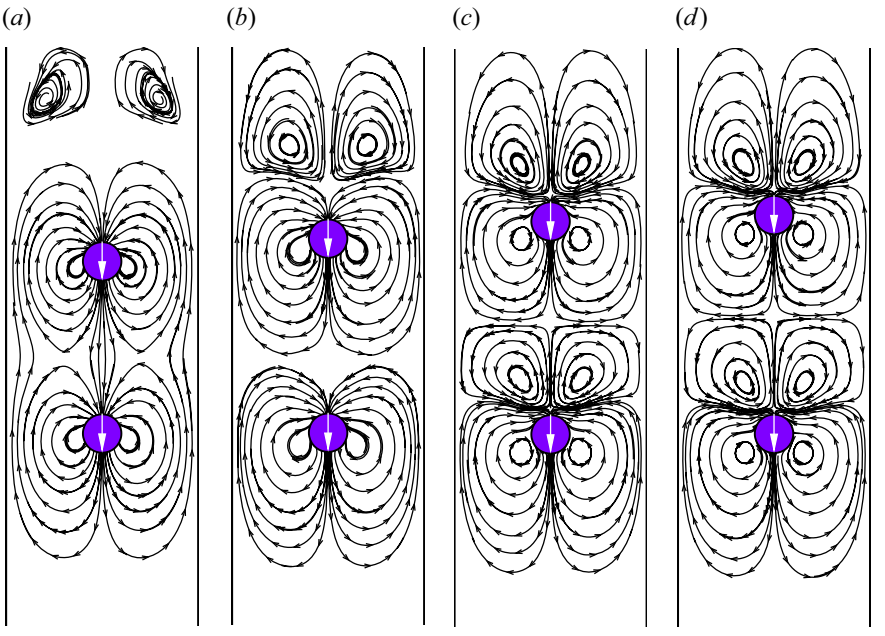

Figure 22. Instantaneous streamlines around settling pushers at $t^* \approx 100$ for $\alpha = 1.2$: (*a*) $\beta = -1$, (*b*) $\beta = -2$, (*c*) $\beta = -4$ and (*d*) $\beta = -5$.

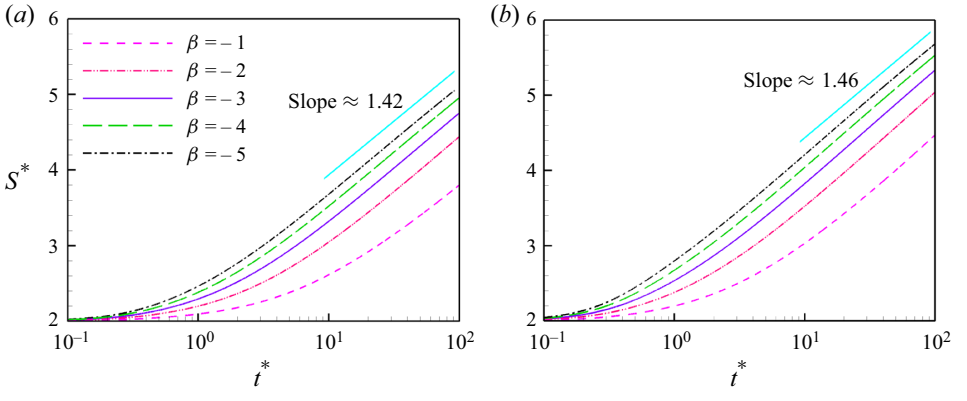

Figure 23. Time history of the normalized distances ($S^* = S/d$) between pushers at different β for (*a*) $\alpha = 0.6$ and (*b*) $\alpha = 1.2$.

a stable doublet is formed, as shown in figure 24. For comparison, the case of non-squirmer particles is also shown in figure 24(*a*).

Our results also indicate that the doublets remain stable for a very long time ($t^* > 500$) before the computations are terminated. They may collapse at the end, but this was not observed. In addition, the doublet formed by squirmers moves much faster than one formed by non-squirmer particles. For instance, the terminal velocity of the doublet for $\alpha = 0.8$ is more than twice that for $\alpha = 0$ (non-squirmer particle).

Another significant feature in the flow around a doublet concerns the absence of the 'leading negative flow' before the puller (figure 24*b–e*). The 'trailing negative flow',

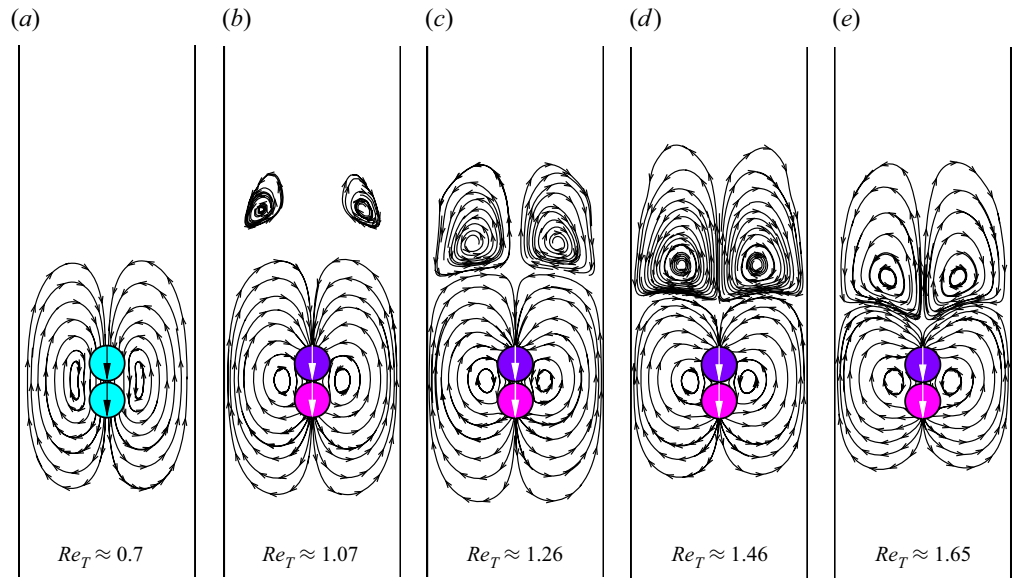

Figure 24. Instantaneous streamlines around settling doublets at steady state: (*a*) $\alpha = 0$ (non-squirmer), (*b*) $\alpha = 0.4$, (*c*) $\alpha = 0.6$, (*d*) $\alpha = 0.8$ and (*e*) $\alpha = 1$. Note that the doublet consists of a pusher ($\beta = -5$, upper) and a puller ($\beta = 5$, lower) for $\alpha > 0$ (the same as below).

however, is visible behind the doublet for all values of α ($\alpha > 0$). To address this issue, we show the instantaneous streamlines and contours of the vertical fluid velocity (normalized by U_g, i.e. $v^* = v/U_g$) during the initial stage at $\alpha = 1.2$ in figure 25. In fact, the 'leading negative flow' is visible before the doublet at $t^* \leq 0.2$, whose intensity decays quickly, as reflected by the magnitude of the vertical fluid velocity (figure 25*a–c*). At $t^* \approx 0.3$, the 'leading negative flow' completely disappears as the doublet is finally formed (figure 25*d*). The reason is simple. The settling velocity of the puller increases as the pusher comes closer to it, driving the 'leading negative flow' farther away from the puller, as shown in figure 25(*a–c*). As the doublet is formed, the puller attains a much larger velocity than that of itself without the presence of a pusher (see figures 8*d* and 24*c*). In addition, the resulting accelerated doublet also drives the 'trailing negative flow' farther behind, whose intensity is significantly reduced (figure 25*d*).

When a puller is initially above a pusher (corresponding to the second situation), the squirmers are always observed to separate from each other at the initial stage, because a pusher moves faster than a puller at the same $|\beta|$. It was shown in § 5.1 that a pusher always achieves a steady state (i.e. SDF) at the channel centreline if it is initially facing downward. However, this may not be the case if a puller is trailing. As shown in figure 12, a puller is very likely to lose its initial symmetrical configuration and subsequently exhibit different patterns; this may alter the steady state of a pusher below, owing to their interactions. To provide a quantitative analysis, we summarized the patterns of interacting squirmers for the second situation, and show them separately in figure 26. It can be seen that the pusher achieves the SDF pattern only at large values of $|\beta|$ (figure 26*a*), because the puller above settles steadily along the channel centreline at the same $|\beta|$ (figure 26*b*). Except for the SDF pattern, the pusher is largely seen to undergo an oscillating motion (LSO or SSO) at intermediate $|\beta|$ values, or to reach an inclined state (SIF or SIR) at small $|\beta|$ values (figure 26*a*). These results are very similar to those of figure 14, which shows the patterns

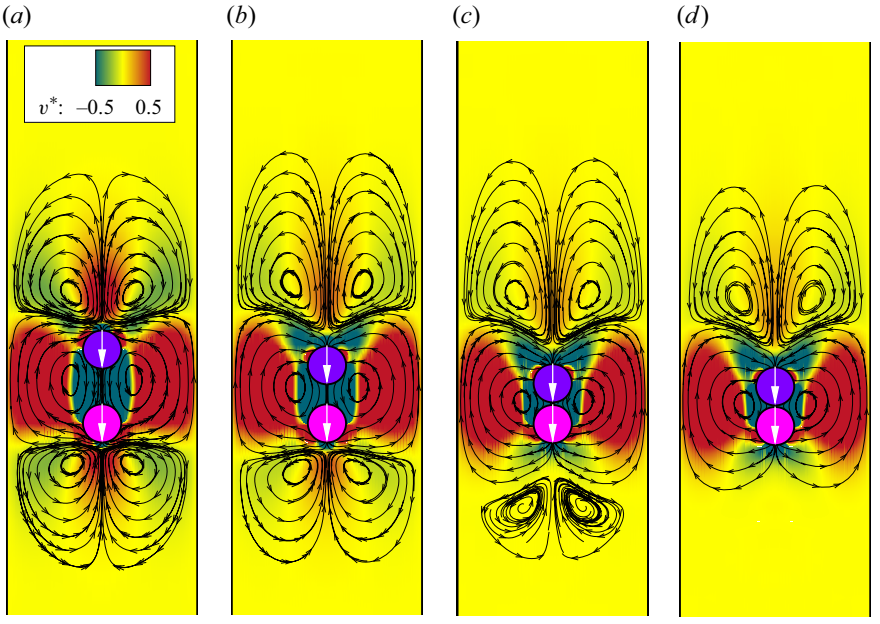

Figure 25. Instantaneous streamlines around two settling squirmers (upper pusher: $\beta = -5$, lower puller: $\beta = 5$) and contours of the vertical fluid velocity during the initial stage for $\alpha = 1.2$: (*a*) $t^* \approx 0.03$, (*b*) $t^* \approx 0.08$, (*c*) $t^* \approx 0.2$ and (*d*) $t^* \approx 0.3$. Note that the vertical velocity of fluid is normalized through $v^* = v/U_g$.

of a pusher with non-zero initial orientations. In contrast, the puller always exhibits an SIF or SIR pattern at these values of $|\beta|$ (figure 26*b*). In particular, the effects of interactions on the motion of the puller are clearly indicated by the results marked with a grey background in figure 26(*b*); these are designated as the LSO or the SSO in figure 12, which summarizes the patterns of a single puller in the same channel. However, the interactions between the squirmers show no influence on the motion of the pusher, in contrast to figure 14. For additional details, we present the results for interacting squirmers (a puller with $\beta = 3$ and pusher with $\beta = -3$) at $\alpha = 0.8$ in figures 27 and 28.

Figure 27 shows the time histories of the horizontal and vertical positions of the squirmers at $t^* \leq 180$. The instantaneous streamlines around the squirmers at the representative times are illustrated in figure 28. It is clear that the pusher loses its stability at $t^* \approx 30$, the same time at which the puller departs from the channel centreline, as indicated by their horizontal positions in figure 27(*a*). Subsequently, the puller quickly changes to an oscillating motion (SSO) near the left wall (figure 28*b*). In contrast, it takes a much longer time ($t^* > 115$) for the pusher to finally realize a LSO motion (figure 27*a*). Figure 28(*c*) shows the corresponding streamlines. Before $t^* = 115$, the distance between the squirmers increases with time as the pusher attains a larger settling velocity, as indicated in figure 27(*b*).

The onset of the LSO motion leads to a significant drop in the settling velocity of the pusher, leading to the fact that the puller settles faster than the pusher. This is confirmed by figure 27(*b*), which shows a decreasing trend in the distance between the squirmers at $t^* > 115$. The puller finally approaches the pusher at $t^* \approx 150$ (figures 27*b* and 28*d*). After contact, the puller turns its orientation upward and ultimately reaches a steady state (SIR) near the right wall (i.e. $X^* = 2$) instead of oscillating. In contrast, the pusher retains its oscillating motion (LSO) in the channel (figures 27*a* and 28*e*). Because the puller has

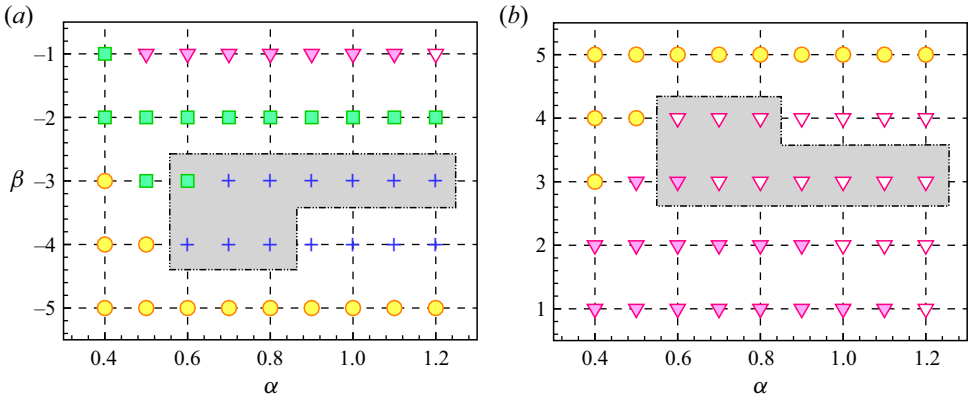

Figure 26. Summary of the patterns of interacting squirmers in the parametric space (α, β) for the situation where a puller is initially placed above a pusher: (*a*) the pusher and (*b*) the puller. As a reminder, each pattern represented by one symbol is reiterated as follows. Circle, SDF; square, SSO; plus, LSO; filled gradient, SIF; open gradient, SIR.

an upward orientation while the pusher remains downward, the two squirmers begin to separate once again ($t^* > 150$), as indicated by figure 27(*b*).

6. Summary

We conducted a numerical study on the motions and interactions of squirmers in a vertical channel using two-dimensional lattice Boltzmann simulations. In addition to the squirmer-type factor (β), another control parameter, namely the self-propelling strength factor, was introduced as $\alpha = U_s/U_g$. In this calculation, U_s denotes the steady swimming velocity of a squirmer, and U_g represents the gravity-driven settling velocity of a non-squirmer particle with the same diameter in a channel in the Stokes flow regime. To better understand the interactions of the squirmers, we first considered the motion of a single squirmer under gravity in a $5d$ (d is the diameter of the squirmers) channel at $0.4 \leq \alpha \leq 1.2$ and $-5 \leq \beta \leq 5$. Based on this, the interactions between two pullers ($\beta > 0$) and two pushers ($\beta < 0$) in the same channel were successively investigated. Finally, we considered the interactions between the pusher and puller. The summary of this study is provided below.

(i) Results show that a single puller reaches a steady state (SDF) along the channel centreline at a large β ($\beta \geq \beta_{c1}$ where β_{c1} is a critical β). At $\beta < \beta_{c1}$, the puller is likely to lose its stability and symmetrical structure, owing to the high-pressure regions on both lateral sides. Accordingly, an LSO motion is eventually achieved for the puller when β is close to another critical value, that is, $\beta \approx \beta_{c2}$. In contrast, it is observed that the puller undergoes an SSO motion at $\beta_{c2} < \beta \leq \beta_{c3}$, where β_{c3} denotes the third critical value of β. Otherwise, the puller achieves an inclined state adjacent to its nearby wall, that is, the SIF or SIR pattern, depending on both α and β. Notably, all of these critical β values (β_{c1}, β_{c2} and β_{c3}) are dependent on α. In particular, an LSO motion rarely occurs for a puller, which differs from an SSO motion in terms of the amplitudes in both the position and orientation of the puller.

The situation is much simpler for a pusher or neutral squirmer, which always reaches a steady state (SDF) when initially facing downward (i.e. at zero initial orientation). A pusher may undergo an oscillating motion (LSO or SSO) or achieve

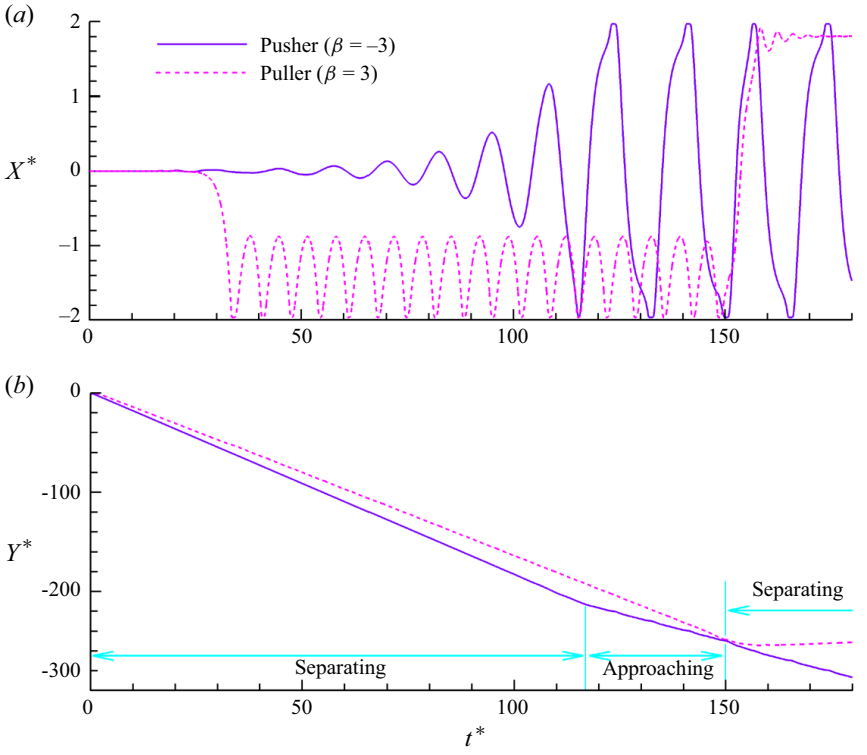

Figure 27. Time history of the positions of the pusher ($\beta = -3$) and the puller ($\beta = 3$) at $\alpha = 0.8$: (a) horizontal component and (b) vertical component.

an inclined state (SIF or SIR) at non-zero initial orientations. However, for the inclined patterns, a distinct difference is found between different squirmers, with a puller facing toward its nearby wall and a pusher facing outward from its nearby wall. This is primarily caused by the different pressure distributions around the different squirmers.

For the SDF pattern, the terminal velocity of a single squirmer increases linearly with α for all types of squirmers. For a fixed α, the pusher always moves faster than the puller, whereas the neutral squirmer is in between. The primary reason is associated with the 'leading negative flow' before a puller and 'trailing negative flow' behind a pusher, which become more significant at larger values of β. A puller experiences a reversed thrust from the 'leading negative flow' as it falls, resulting in a decrease in its settling velocity. However, the 'trailing negative flow' does the opposite to a pusher. There is no 'negative flow' for a neutral squirmer. Different types of squirmers show different trends in their terminal velocities with increasing channel width.

(ii) The interactions between two pullers are complex. The SDF pattern observed for a single puller at a large β does not exist in this situation. For most cases of two squirmers ($-5 \leq \beta \leq 5$) released in a channel, they may interact with each other for a certain time, but in the end, they settle in the channel separately while exhibiting the same or different patterns of motion. In general, our simulations show that both pullers begin to attract each other once they are released from rest, owing to the low-pressure regions between them. They may quickly come into contact. After that,

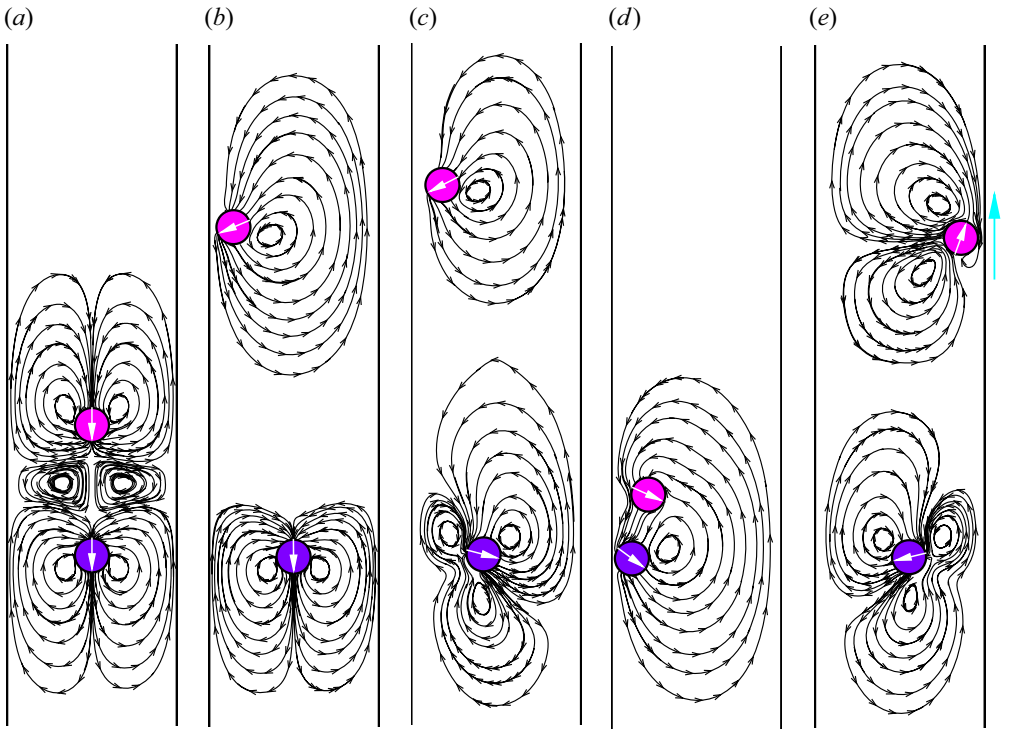

Figure 28. Instantaneous streamlines around the settling squirmers at $\alpha = 0.8$ at different times showing the interactions between a pusher ($\beta = -3$) and puller ($\beta = 3$): (*a*) $t^* \approx 10$, (*b*) $t^* \approx 40$, (*c*) $t^* \approx 130$, (*d*) $t^* \approx 150$ and (*e*) $t^* \approx 160$.

the upper puller attains an upward orientation and reaches an inclined state (SIF or SIR, respectively). However, the lower puller undergoes an LSO motion at $\beta \approx \beta_{c2}$, similar to the case of a single puller. In particular, the SSO motion occurs only at some values of β that are slightly larger than β_{c2}. Otherwise, the lower puller exhibits an SIF or SIR pattern.

(iii) In comparison with pullers, the interactions between two pushers are simple. Only the SDF pattern is observed for both pushers in all studied cases. Pushers always repel each other and begin to separate once they are released, owing to the high-pressure regions between them. In addition, the 'trailing negative flow' behind the lower pusher, which becomes strong at larger values of β, is seen to further increase the separation between the pushers.

(iv) Regarding the interactions between a puller and pusher, two situations were considered: a pusher initially leading a puller and its opposite. For both cases, we assumed that both squirmers had the same $|\beta|$. In the former situation, the pusher always approaches the puller, because the pusher moves faster than a puller at the same $|\beta|$. Then, a stable doublet is quickly formed, and shows a noticeably large settling velocity compared with the case of non-squirmer particles or a single squirmer. In contrast, the latter situation is quite different. Both squirmers separate at the initial stage. However, apart from the SDF pattern at large $|\beta|$ values observed for a single pusher at all values of $|\beta|$, the pusher may exhibit an oscillating motion (LSO or SSO) at an intermediate $|\beta|$ or an inclined state (SIF or SIR) at a small $|\beta|$, as a result of its interactions with the puller. The most significant effect of the interactions

on the puller is that there is no oscillating motion (LSO or SSO) for it, as compared with the case of a single puller undergoing the LSO or SSO motion at intermediate values of $|\beta|$. The reason for this is briefly explained below. The puller quickly turns into an oscillating motion as it separates from the pusher. The pusher loses stability and requires a long time to realize an oscillating motion. This significantly reduces the settling velocity. Subsequently, the puller approaches it. After contact, the puller turns its orientation upward, and ultimately reaches a steady state adjacent to its nearby wall. However, the contact does not change the orientation of the pusher. In other words, it remains downward, and continues to oscillate.

(v) It should be more interesting to perform three-dimensional analysis of squirmers settling under gravity in a tube. In addition to the patterns exhibited by circular squirmers, the extra dimension may allow different dynamical features to occur for spherical squirmers (e.g. the spiral or zigzagging trajectory). On the other hand, the gravity-driven motion of interacting squirmers at moderate Reynolds numbers where the fluid inertia play an important role deserves more efforts. This becomes our future work.

Funding. This study was supported by the National Natural Science Foundation of China (nos 12132015 and 11972336).

Declaration of interests. The authors report no conflict of interest.

Author ORCIDs.
Deming Nie https://orcid.org/0000-0002-7793-2725;
Jianzhong Lin https://orcid.org/0000-0001-8418-1176;
Zhenyu Ouyang https://orcid.org/0000-0002-2481-0994.

References

Ahana, P. & Thampi, S.P. 2019 Confinement induced trajectory of a squirmer in a two dimensional channel. *Fluid Dyn. Res.* **51**, 065504.

Aidun, C.K., Lu, Y. & Ding, E. 1998 Direct analysis of particulate suspensions with inertia using the discrete Boltzmann equation. *J. Fluid Mech.* **373**, 287–311.

Berke, A.P., Turner, L., Berg, H.C. & Lauga, E. 2008 Hydrodynamic attraction of swimming microorganisms by surfaces. *Phys. Rev. Lett.* **101**, 038102.

Blake, J.R. 1971*a* A spherical envelope approach to ciliary propulsion. *J. Fluid Mech.* **46**, 199–208.

Blake, J.R. 1971*b* Self propulsion due to oscillations on the surface of a cylinder at low Reynolds number. *Bull. Austral. Math. Soc.* **5**, 255–264.

Chisholm, N., Legendre, D., Lauga, E. & Khair, A. 2016 A squirmer across Reynolds numbers. *J. Fluid Mech.* **796**, 233–256.

Di Leonardo, R., Angelani, L., Dell'Arciprete, D. & Di Fabrizio, E. 2010 Bacterial ratchet motors. *Proc. Natl Acad. Sci. USA* **107**, 9541–9545.

Drescher, K., Leptos, K.C., Tuval, I., Ishikawa, T., Pedley, T.J. & Goldstein, R.E. 2009 Dancing volvox: hydrodynamic bound states of swimming algae. *Phys. Rev. Lett.* **102**, 168101.

Elgeti, J., Winkler, R.G. & Gompper, G. 2015 Physics of microswimmers—single particle motion and collective behavior: a review. *Rep. Prog. Phys.* **78**, 056601.

Fadda, F., Molina, J.J. & Yamamoto, R. 2020 Dynamics of a chiral swimmer sedimenting on a flat plate. *Phys. Rev.* E **101**, 052608.

Fenchel, T. & Finlay, B.J. 1986 Photobehavior of the ciliated protozoon Loxodes: taxic, transient, and kinetic responses in the presence and absence of oxygen. *J. Protozool.* **33**, 139–145.

Feng, J., Hu, H.H. & Joseph, D.D. 1994 Direct simulation of initial value problems for the motion of solid bodies in a Newtonian fluid. Part 1. Sedimentation. *J. Fluid Mech.* **261**, 95–134.

Friedrich, B.M., Riedel-Kruse, I.H., Howard, J. & Jülicher, F. 2010 High-precision tracking of sperm swimming fine structure provides strong test of resistive force theory. *J. Expl Biol.* **213**, 1226–1234.

GEYER, V.F., JÜLICHER, F., HOWARD, J. & FRIEDRICH, B.M. 2013 Cell-body rocking is a dominant mechanism for flagellar synchronization in a swimming alga. *Proc. Natl Acad. Sci. USA* **110**, 18058–18063.

GLOWINSKI, R., PAN, T.-W., HESLA, T.I., JOSEPH, D.D. & PERIAUX, J. 2001 A fictitious domain approach to the direct numerical simulation of incompressible viscous flow past moving rigid bodies: application to particulate flow. *J. Comput. Phys.* **169**, 363–426.

GÖTZE, I.O. & GOMPPER, G. 2010 Mesoscale simulations of hydrodynamic squirmer interactions. *Phys. Rev.* E **82**, 041921.

TEN HAGEN, B., KÜMMEL, F., WITTKOWSKI, R., TAKAGI, D., LÖWEN, H. & BECHINGER, C. 2014 Gravitaxis of asymmetric self-propelled colloidal particles. *Nat. Commun.* **5**, 4829.

HAPPEL, J. & BRENNER, H. 1965 *Low Reynolds Number Hydrodynamics*. Prentice-Hall.

HILL, N.A. & PEDLEY, T.J. 2005 Bioconvection. *Fluid Dyn. Res.* **37**, 1–20.

HU, J., WYSOCK, A., WINKLER, R.G. & GOMPPER, G. 2015 Physical sensing of surface properties by microswimmers – directing bacterial motion via wall slip. *Sci. Rep.* **5**, 9586.

HWANG, Y. & PEDLEY, T.J. 2014 Bioconvection under uniform shear: linear stability analysis. *J. Fluid Mech.* **738**, 522–562.

ISHIKAWA, T. & HOTA, M. 2006 Interaction of two swimming Paramecia. *J. Expl Biol.* **209**, 4452–4463.

ISHIKAWA, T., LOCSEI, J.T. & PEDLEY, T.J. 2008 Development of coherent structures in concentrated suspensions of swimming model micro-organisms. *J. Fluid Mech.* **615**, 401–431.

ISHIKAWA, T., SEKIYA, G., IMAI, Y. & YAMAGUCHI, T. 2007 Hydrodynamic interactions between two swimming bacteria. *Biophys. J.* **93**, 2217–2225.

ISHIKAWA, T., SIMMONDS, M.P. & PEDLEY, T.J. 2006 Hydrodynamic interaction of two swimming model micro-organisms. *J. Fluid Mech.* **568**, 119–160.

JALALI, M.A., KHOSHNOOD, A. & ALAM, M.-R. 2015 Microswimmer-induced chaotic mixing. *J. Fluid Mech.* **779**, 669–683.

KHAIR, A.S. & CHISHOLM, N.G. 2014 Expansions at small Reynolds numbers for the locomotion of a spherical squirmer. *Phys. Fluids* **26**, 011902.

KLINDT, G.S. & FRIEDRICH, B.M. 2015 Flagellar swimmers oscillate between pusher- and puller-type swimming. *Phys. Rev.* E **92**, 063019.

KOCH, D. & SUBRAMANIAN, G. 2011 Collective hydrodynamics of swimming microorganisms: living fluids. *Annu. Rev. Fluid Mech.* **43**, 637–659.

KYOYA, K., MATSUNAGA, D., IMAI, Y., OMORI, T. & ISHIKAWA, T. 2015 Shape matters: near-field fluid mechanics dominate the collective motions of ellipsoidal squirmers. *Phys. Rev.* E **92**, 063027.

LALLEMAND, P. & LUO, L.S. 2003 Lattice Boltzmann method for moving boundaries. *J. Comput. Phys.* **184**, 406–421.

LAUGA, E. & POWERS, T. 2009 The hydrodynamics of swimming microorganisms. *Rep. Prog. Phys.* **72**, 096601.

LI, G.J. & ARDEKANI, A.M. 2014 Hydrodynamic interaction of micorswimmers near a wall. *Phys. Rev.* E **90**, 013010.

LI, G.J., OSTACE, A. & ARDEKANI, A.M. 2016 Hydrodynamic interaction of swimming organisms in an inertial regime. *Phys. Rev.* E **94**, 053104.

LIGHTHILL, M.J. 1952 On the squirming motion of nearly spherical deformable bodies through liquids at very small Reynolds numbers. *Commun. Pure Appl. Maths* **5**, 109–118.

LIN, Z.W. & GAO, T. 2019 Direct-forcing fictitious domain method for simulating non-Brownian active particles. *Phys. Rev.* E **100**, 013304.

LUSHI, E., WIOLAND, H. & GOLDSTEIN, R. 2014 Fluid flows generated by swimming bacteria drive self-organization in confined fluid suspensions. *Proc. Natl Acad. Sci. USA* **111**, 9733–9738.

MATAS-NAVARRO, R., GOLESTANIAN, R., LIVERPOOL, T.B. & FIELDING, S.M. 2014 Hydrodynamic suppression of phase separation in active suspensions. *Phys. Rev.* E **90**, 032304.

MEI, R., YU, D., SHYY, W. & LUO, L.-S. 2002 Force evaluation in the lattice Boltzmann method involving curved geometry. *Phys. Rev.* E **65**, 041203.

MIRZAKHANLOO, M., JALALI, M.A. & ALAM, M.R. 2018 Hydrodynamic choreographies of microswimmers. *Sci. Rep.* **8**, 3670.

MOGAMI, Y., ISHII, J. & BABA, S.A. 2001 Theoretical and experimental dissection of gravity-dependent mechanical orientation in gravitactic microorganisms. *Biol. Bull.* **201**, 26–33.

MORE, R.V. & ARDEKANI, A.M. 2021 Hydrodynamic interactions between swimming microorganisms in a linearly density stratified fluid. *Phys. Rev.* E **103**, 013109.

NAJAFI, A., RAAD, S.S.H. & YOUSEFI, R. 2013 Self-propulsion in a low-Reynolds-number fluid confined by two walls of a microchannel. *Phys. Rev.* E **88**, 045001.

NIE, D.M., GUAN, G. & LIN, J.Z. 2021 Interaction between two unequal particles at intermediate Reynolds numbers: a pattern of horizontal oscillatory motion. *Phys. Rev.* E **103**, 013105.
NIE, D.M. & LIN, J.Z. 2019 Discontinuity in the sedimentation system with two particles having different densities in a vertical channel. *Phys. Rev.* E **99**, 053112.
NIE, D.M. & LIN, J.Z. 2020 Simulation of sedimentation of two spheres with different densities in a square tube. *J. Fluid Mech.* **896**, A12.
NTEFIDOU, M., ISEKI, M., WATANABE, M., LEBERT, M. & HÄDER, D.-P. 2003 Photoactivated adenylyl cyclase controls phototaxis in the flagellate Euglena gracilis. *Plant Physiol.* **133**, 1517–1521.
OUYANG, Z.Y. & LIN, J.Z. 2022 Behaviors of a settling microswimmer in a narrow vertical channel. *Powder Technol.* **398**, 117042.
OUYANG, Z.Y., LIN, J.Z. & KU, X.K. 2018 The hydrodynamic behavior of a squirmer swimming in power-law fluid. *Phys. Fluids* **30**, 083301.
PAPAVASSILIOU, D. & ALEXANDER, G.P. 2017 Exact solutions for hydrodynamic interactions of two squirming spheres. *J. Fluid Mech.* **813**, 618–646.
PEDLEY, T.J. & KESSLER, J.O. 1992 Hydrodynamic phenomena in suspensions of swimming microorganisms. *Annu. Rev. Fluid Mech.* **24**, 313–358.
POLIN, M., TUVAL, I., DRESCHER, K., GOLLUB, J.P. & GOLDSTEIN, R.E. 2009 Chlamydomonas swims with two "gears" in a eukaryotic version of run-and-tumble locomotion. *Science* **325**, 487–490.
POOLEY, C.M., ALEXANDER, G.P. & YEOMANS, J.M. 2012 Hydrodynamic interaction between two swimmers at low Reynolds number. *Phys. Rev. Lett.* **99**, 228103.
QI, K., WESTPHAL, E., GOMPPER, G. & WINKLER, R.G. 2022 Emergence of active turbulence in microswimmer suspensions due to active hydrodynamic stress and volume exclusion. *Commun. Phys.* **5**, 49.
QIAN, Y.H. 1992 Lattice BGK models for Navier–Stokes equation. *Europhys. Lett.* **17**, 479–484.
ROBERTS, A.M. 2010 The mechanics of gravitaxis in Paramecium. *J. Expl Biol.* **213**, 4158–4162.
RÜHLE, F., BLASCHKE, J., KUHR, J.T. & STARK, H. 2018 Gravity-induced dynamics of a squirmer microswimmer in wall proximity. *New J. Phys.* **20**, 025003.
SAINTILLAN, D. 2018 Rheology of active fluids. *Annu. Rev. Fluid Mech.* **50**, 563–592.
SENGUPTA, A., CARRARA, F. & STOCKER, R. 2017 Phytoplankton can actively diversify their migration strategy in response to turbulent cues. *Nature* **543**, 555–558.
SHEN, Z., WÜRGER, A. & LINTUVUORI, J.S. 2018 Hydrodynamic interaction of a self-propelling particle with a wall. *Eur. Phys. J.* E **41**, 39.
SOKOLOV, A., APODACA, M.M., GRZYBOWSKI, B.A. & ARANSON, I.S. 2009 Swimming bacteria power microscopic gears. *Proc. Natl Acad. Sci. USA* **107**, 969–974.
SOKOLOV, A. & ARANSON, I.S. 2012 Physical properties of collective motion in suspensions of bacteria. *Phys. Rev. Lett.* **109**, 248109.
THEERS, M., WESTPHAL, E., GOMPPER, G. & WINKLER, R.G. 2016 Modeling a spheroidal microswimmer and cooperative swimming in a narrow slit. *Soft Matt.* **35**, 7372–7385.
THEERS, M., WESTPHAL, E., QI, K., WINKLER, R.G. & GOMPPER, G. 2018 Clustering of microswimmers: interplay of shape and hydrodynamics. *Soft Matt.* **14**, 8590–8603.
WANG, S. & ARDEKANI, A. 2012 Inertial squirmer. *Phys. Fluids* **24**, 101902.
WANG, S. & ARDEKANI, A. 2015 Biogenic mixing induced by intermediate Reynolds number swimming in stratified fluids. *Sci. Rep.* **5**, 17448.
WIOLAND, H., LUSHI, E. & GOLDSTEIN, R. 2016 Directed collective motion of bacterial under channel confinement. *New J. Phys.* **18**, 075002.
WOLFF, K., HAHN, A.M. & STARK, H. 2013 Sedimentation and polar order of active bottom-heavy particles. *Eur. Phys. J.* E **36**, 43.